Acceleration, Creation, and Depletion of Wind-Driven, Baroclinic Rossby Waves over an Ocean Ridge

RÉMI TAILLEUX AND JAMES C. MCWILLIAMS

Institute of Geophysics and Planetary Physics, University of California, Los Angeles, Los Angeles, California

ABSTRACT

The influences of topography on the propagation, spatial patterns, and amplitude variations of long baroclinic Rossby waves are investigated with a wind-forced, two-layer model above a midocean ridge. With steep topography the evolution equation for the baroclinic mode is shown to differ from that for a flat bottom in several ways: 1) The phase speed is systematically faster by the factor H/H_2, where H is the total ocean depth and H_2 is the lower layer thickness, though the propagation remains westward and nearly nondispersive; 2) an effectively dissipative transfer to the barotropic mode occurs whenever the baroclinic mode is locally parallel to f/H contours, where f is the Coriolis frequency; and 3) the wind-forced response is amplified in proportion to the topographic steepness, $(f/H)(dH/dx)/(df/dy)$, for a longitudinally varying topography, which can be a large factor, but the amplification is only by the modest factor H/H_2 for a latitudinally varying topography. Effects 2 and 3 are the result of energy exchanges to and from the barotropic mode, respectively. Effect 3 causes freely propagating, baroclinic Rossby waves to be generated west of the ridge. These effects collectively cause distortions of the baroclinic wave pattern as it traverses the ridge. These effects account qualitatively for several features seen in altimetric measurements in the vicinity of major topographic features: an increase in variance of baroclinic signals on the west side, an enhanced phase speed overall (compared to flat-bottom waves), and an abrupt change in the phase speed at midocean ridges.

1. Introduction

We investigate the effects of bottom topography on the creation, propagation, amplification, depletion, and distortion of baroclinic Rossby waves. Our work is motivated in part by the Chelton and Schlax (1996) analysis of TOPEX/Poseidon altimetric measurements showing that steep topographic features significantly alter the phase speed and amplitude of low-frequency signals associated with baroclinic Rossby waves. For instance, Fig. 2 in Chelton and Schlax (1996) demonstrates that propagating patterns in the sea surface height are larger in amplitude west of major topographic features, such as the Emperor Seamounts at 39°N, 170°E, the southeast flank of Hess Rise at 32°N, 175°E, and the Hawaiian Ridge at 21°N, 155°W; similar results are found for the North Atlantic (Tokmakian and Challenor 1993; Schlax and Chelton 1994). In some instances, the waves seem to amplify over the midocean topography, while in others they seem to be created. In the North Atlantic the phase speed of baroclinic Rossby waves appears to change abruptly over the midocean ridge.

Also shown by Chelton and Schlax is that the baroclinic Rossby waves propagate faster than predicted by the standard linear flat-bottom theory, outside the tropical band (10°S–10°N), with an amplification factor seemingly increasing poleward. Killworth et al. (1997) argues that the modification of the background planetary potential vorticity field by the mean, large-scale circulation is the most likely cause of the difference. In principle, a mean flow can speed up, slow down, or even reverse the propagation of Rossby waves. According to Dewar (1998) and de Szoeke and Chelton (1999), the reason for speedup might be due to to the existence of homogeneous potential vorticity regions below the thermocline associated with the vertical shear. However, despite providing some improvement over the standard theory, the theory of Killworth et al. (1997, their Fig. 1) still predicts speeds that are systematically too low, especially in the Southern Hemisphere. It also provides no improvement in the band (10°S–10°N), where these wave theories predict systematically high speeds. This may be due to the neglect of the meridional shear of mean zonal currents, which reduces the potential vorticity gradient, hence the effective β value and Rossby wave speed (Philander 1979; Chang and Philander 1989; Zheng et al. 1994). Other mechanisms related to wave nonlinearity, forcing, and dissipation are rejected in Killworth et al. (1997).

Corresponding author address: Rémi Tailleux, LMD–UPMC Paris 6, Case Courrier 99, 4 Place Jussieu, Paris Cedex 75252, France.
E-mail: tailleux@lmg.jussieu.fr

Topography deserves attention as an influence because previous theories suggest that it can systematically enhance the phase speed of first-baroclinic Rossby waves. In a two-layer model, Rhines (1977) and Veronis (1981) use a WKB approach to show that the propagation of long Rossby waves over a steep topography remains westward and nondispersive, as in the flat-bottom case, but faster by the factor $H/H_2 > 1$ [i.e., $c = g'\beta H_1/f^2$ instead of the standard $c = g'\beta H_1(H - H_1)/f^2H$, where H_1 is upper layer thickness, H is total depth, f is Coriolis frequency, $\beta = df/dy$, $g' = g\Delta\rho/\rho$ is the reduced gravitational acceleration, and $\Delta\rho$ is the density difference across the layer interface]. In this steep limit, achieved when the topographic β effect $f\|\nabla H\|/H$ is greater than the planetary β, the waves are trapped in the upper layer and propagate as if unaffected by the topography. The existence of top-trapped, propagating modes is a well-known results of WKB theory for baroclinic Rossby waves over topography (e.g., Samelson 1992; Reznik and Tsybaneva 1994; Straub 1994; Hallberg 1997). In this case, baroclinic Rossby waves have the same phase speed as in a 1.5-layer model (i.e., a two-layer model with a resting deep layer, for which decoupling with the topography occurs trivially).

The use of a 1.5-layer model is common among physical oceanographers. One rationalization stems from the observation that velocities and pressure gradients are generally larger near the ocean surface than near the bottom, a situation sometimes called ''pressure compensation'' (e.g., Mellor and Wang 1996). Pressure compensation sometimes develops in the absence of topography. It occurs in wind-forced gyre spinup (Anderson and Gill 1975; Anderson and Killworth 1977), regardless of the nature of the topography. It also occurs for a baroclinic eddy propagating over a flat bottom (McWilliams et al. 1986), with an accompanying speed enhancement. From these examples it is tempting to hypothesize that pressure compensation is widespread, as would then be its associated phase speed enhancement. This hypothesis is an attractive alternative or complement to the mean-flow theory in interpreting the results of Chelton and Schlax (1996). As yet, the speed enhancement by compensation has not been estimated for a continuously stratified fluid.

How are baroclinic Rossby waves generated, and where are they amplified and depleted? In the theory of White (1977), a time-varying, zonally uniform wind generates zonally propagating waves at the eastern boundary in order to assure no normal flow. The numerical solutions in Barnier (1988) show that free baroclinic Rossby waves can be generated in the ocean interior by the wind or by an ocean ridge. Once the waves are generated, they undergo changes in shape by the action of the wind forcing and, for short wavelengths, by dispersive effects. Viscous damping and bottom drag dissipate the waves (e.g., see Qiu et al. 1997). In Sakamoto and Yamagata (1997), a baroclinic eddy is depleted while propagating over a ridge as a result of topographic coupling with the barotropic mode, which the authors interpret in terms of JEBAR (joint effect of baroclinicity and relief). In Barnier (1988), the creation of baroclinic Rossby waves over a ridge indicates the possibility of energy transfer from the barotropic mode to the baroclinic one. In Sakamoto and Yamagata (1997), the depletion of a baroclinic eddy over a ridge suggests that the energy transfer can also occur in the opposite direction.

One interpretive issue related to JEBAR is how topography couples the standard modes to produce new wave modes in the absence of forcing and dissipation. Another issue is whether these new modes are coupled or independent. The first issue is addressed with WKB theory in, for example, Rhines (1970), Charney and Flierl (1981), Straub (1994), Samelson (1992), and Reznik and Tsybaneva (1994). These studies mainly focus on the effect of topography in the locally valid dispersion relation and the vertical modal structure. Analyses of the phase speed over a latitudinally varying topography in a continuously stratified fluid are given in Rhines (1970) and for an arbitrary (but smooth) topography in the long-wave limit in Killworth and Blundell (1999). These papers predict that the ratio of wave speeds with and without topography should lie within the interval (4/9 to 4); however, by calculating rays emanating from eastern boundaries over realistic but highly smoothed topography, Killworth and Blundell (1999) concludes against a net enhancement of phase speed, in contrast with the findings of Rhines (1977) and Veronis (1981) for a steep topography [a condition rarely encountered in Killworth and Blundell (1999) where only very smooth topography is considered].

The second JEBAR issue, related to the coupling of WKB modes, has not received much attention so far. The main reason is that an absence of coupling between wave modes is usually assumed a priori in the WKB approach. The single-mode assumption is indeed essential to the success of action–conservation theorems for instance. Such an assumption implicitly requires that the WKB approximation remains uniformly valid throughout the domain considered. However, this needs not be the case. Evidence that the WKB modes are, in fact, unavoidably coupled is implicitly contained in the numerical simulations by Barnier (1988), Sakamoto and Yamagata (1997), or in the ones presented in this paper. In these papers, one usually starts from a situation with a single standard wave mode in the flat eastern part of the basin and ends up with two distinct standard wave modes in the flat western part, the middle part of the basin being occupied by some topographic features over which wave modes are not as unambiguously defined as over the flat-bottom parts. If there was no mode coupling over the topographic features, only one single mode would be obtained in the western part by the action conservation principle. From a theoretical viewpoint, the coupling of WKB modes must be intrinsically linked to the breakdown of WKB theory. We are not

aware, however, of previous works describing the general circumstances of this link. A first step toward a theoretical understanding of WKB-mode coupling is achieved by Hallberg (1997) who suggests that the breakdown of WKB theory is likely to occur near turning points. Such points correspond to a region in wavenumber space where the dispersion curve $\omega = $ const of the mode considered exhibits a sharp gradient. The physical interpretation given by Hallberg is that the Rossby wave energy cannot stay within a single wave mode at a turning point without violating mass conservation. On this basis, he is able to derive heuristic estimates for the amplitude of the additional mode required. In this respect, this case is different from the previously known case of coastal waves where the switch of one type of mode to a different type occurs with the energy staying within a single mode (Allen and Romea 1980). In contrast, Killworth and Blundell (1999) assumes explicitly that no energy scattering between WKB modes occurs and makes ray calculations for the world oceans that exhibit caustics, but no turning points. In this case, the absence of turning points seems to be due to the lack of dispersive effects (P. D. Killworth 1999, personal communication). Since caustics are also known to be associated with a local breakdown of WKB theory, they may also be linked to WKB-mode coupling, although the generally accepted idea is that they correspond to a transition region between a one-mode solution to a no-mode solution (e.g., Lighthill 1978).

Since the above remarks suggest that even the WKB modes are not uncoupled over topography, one may as well deal with the standard modes whose definition has the advantage to be independent of position. For this reason, we shall deal in this paper only with the standard baroclinic and barotropic modes, not with their generalized WKB counterparts. A simple theoretical model is constructed to address the above JEBAR issues for forced waves. We seek insight into the mechanisms associated with the generation, propagation, and decay of baroclinic Rossby waves that are strongly affected by steep topography. Since a WKB theory applies to unforced waves in a slowly varying medium, we rely primarily on numerical solutions of planetary geostrophic equations appropriate to large-scale waves; not surprisingly, though, our solutions show some similarities to those derived by a WKB approach. The material is organized as follows: the model equations are in section 2, theoretical analyses are in sections 3 and 4, illustrative numerical solutions are in section 5, and concluding remarks are in section 6.

2. Model formulation

To focus on the interaction between the barotropic and baroclinic modes in the presence of topography, the stratification is modeled as a thin layer of density ρ_1 overlying a deep layer of greater density ρ_2 (Fig. 1).
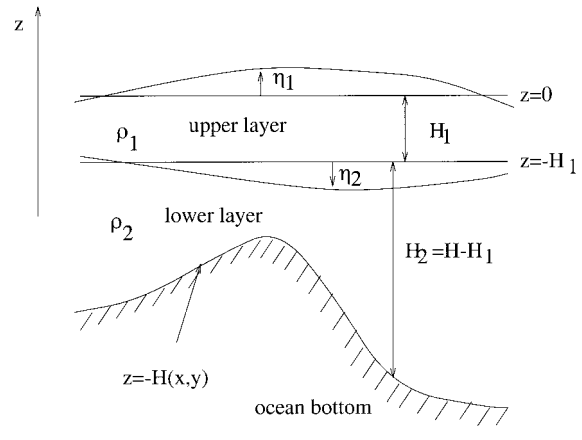

FIG. 1. Geometry and notation for the two-layer model.

The unperturbed thicknesses of these layers are denoted by H_1 and $H_2 = H - H_1$ respectively, with $H(x, y)$ the total ocean depth. We denote the perturbation elevations of the surface and interface by η_1 and η_2, respectively. Thus, the total layer thicknesses are $h_1 = H_1 + \eta_1 - \eta_2$ and $h_2 = H_2 + \eta_2$. For small disturbances to a stratified state of rest, we use the linearized primitive equations for the layer horizontal transports $U_i = h_i \mathbf{u}_i \approx H_i \mathbf{u}_i$:

$$\frac{\partial \mathbf{U}_1}{\partial t} + f\hat{\mathbf{z}} \times \mathbf{U}_1 + H_1 \boldsymbol{\nabla} p_1 = \boldsymbol{\tau} - r\mathbf{U}_1 \qquad (1)$$

$$\frac{\partial(\eta_1 - \eta_2)}{\partial t} + \text{div}\mathbf{U}_1 = 0 \qquad (2)$$

$$\frac{\partial \mathbf{U}_2}{\partial t} + f\hat{\mathbf{z}} \times \mathbf{U}_2 + H_2 \boldsymbol{\nabla} p_2 = -r\mathbf{U}_2 \qquad (3)$$

$$\frac{\partial \eta_2}{\partial t} + \text{div}\mathbf{U}_2 = 0. \qquad (4)$$

The layer pressures are related to the surface and interface displacements by $p_1 = g\eta_1$ and $p_2 = g(\eta_1 + \epsilon\eta_2)$; r is a damping rate representing viscous processes.

For inviscid interior solutions that are large scale and slowly varying in time, the above equations can be approximated by the planetary geostrophic equations, obtained by making the rigid-lid approximation and assuming that the horizontal velocity is in geostrophic equilibrium below the surface Ekman layer [i.e., friction and the time derivatives in (1) and (3), as well as the term $\partial_t \eta_1$ in (2), are neglected: see Colin de Verdière 1988]. As a result of the rigid-lid approximation, the vertically integrated horizontal transport is divergenceless, and hence can be expressed in terms of a streamfunction by $\mathbf{U} = \mathbf{U}_1 + \mathbf{U}_2 = \hat{\mathbf{z}} \times \boldsymbol{\nabla}\Psi$. The vertically integrated momentum equations can be expressed in terms of Ψ as follows:

$$-f\boldsymbol{\nabla}\Psi + H_1\boldsymbol{\nabla} p_1 + H_2\boldsymbol{\nabla} p_2 = \boldsymbol{\tau}. \qquad (5)$$

After some algebra, equations for Ψ and the baroclinic pressure $\tilde{p} = p_2 - p_1 = g'\eta_2$ only can be obtained, given by

$$J\left(\Psi, \frac{f}{H}\right) = \text{curl}\left(\frac{\tau}{H}\right) + \frac{H_1}{H^2}J(\tilde{p}, H) \qquad (6)$$

$$\frac{\partial \tilde{p}}{\partial t} + g'J\left(\tilde{p}, \frac{H_1 H_2}{fH}\right) = g' \, \text{curl}\left(\frac{H_2 \tau}{fH}\right) + \frac{g'H_1}{H^2}J(H, \Psi). \qquad (7)$$

Equation (6) generalizes the classical Sverdrup relation (Sverdrup 1947) by accounting for the bottom pressure torque (or JEBAR effect). It is obtained by taking the curl of Eq. (5) divided by H. Equation (7) is the evolution equation for the baroclinic pressure, obtained from (4) by using $\mathbf{U}_2 = (H_2/H)\hat{\mathbf{z}} \times \nabla\Psi + (H_2/H)\hat{\mathbf{z}} \times \tau/f + H_1 H_2/(fH)\hat{\mathbf{z}} \times \nabla\tilde{p}$ that results from eliminating p_1 between (1) and (3). In the flat-bottom case, Eqs. (7) and (6) are uncoupled, so Ψ and $\tilde{p}$ are related to the standard barotropic and baroclinic modes. Alternatively, Eq. (7) can be combined with (6) to be rewritten under the form

$$\frac{\partial \tilde{p}}{\partial t} - \frac{g'\beta H_1 H_2}{f^2 H}\frac{\partial \tilde{p}}{\partial x} = \frac{g'H_2}{H}w_E - \frac{g'H_1}{fH}\left[\beta\frac{\partial \Psi}{\partial x} - \text{curl}\tau\right], \qquad (8)$$

using $H \, \text{curl}(\tau/H) = \text{curl}\tau + (\hat{\mathbf{z}} \times \tau) \cdot \nabla H/H$, $\text{curl}(H_2\tau/Hf) = (H_2/H)w_E + H_1(\hat{\mathbf{z}} \times \tau) \cdot \nabla H/fH^2$, and $fJ(H, \Psi)/H^2 = J(\Psi, f/H) - (\beta/H)\partial_x\Psi$; $w_E = \text{curl}(\tau/f)$ is the classical Ekman pumping velocity. An equation for the surface pressure in terms of $\tilde{p}$ can be obtained by taking the curl of (5) divided by f, yielding

$$J\left(\frac{H}{f}, p_1\right) + J\left(\frac{H_2}{f}, \tilde{p}\right) = w_E. \qquad (9)$$

Equation (9) can also be seen as an equation for p_2 by using $p_1 = p_2 - \tilde{p}$. Another possibility to determine p_1 and p_2 as a function of $\tilde{p}$ and Ψ would be to integrate (5) from the eastern boundary.

It would be a mistake to regard Eqs. (7) and (8) as forced wave equations—in the first case with characteristics $H_1 H_2/fH = \text{const.}$, in the second case with zonal characteristics—because the signal propagation is determined by the coupling between Eqs. (6) and (7), as analyzed below. Such a mistake would be similar to the one often made by regarding JEBAR as a forcing term in the equation for the barotropic mode, as a result of assuming the stratification known when in fact the latter is to be determined as part of the solution.

3. Effects of topography on the baroclinic mode

a. Topography varying only with latitude

In this case, the vorticity balance (6) reduces to

$$\frac{d}{dy}\left(\frac{f}{H}\right)\frac{\partial \Psi}{\partial x} = \text{curl}\left(\frac{\tau}{H}\right) + \frac{H_1}{H^2}H'(y)\frac{\partial \tilde{p}}{\partial x}, \qquad (10)$$

where $H'(y) = dH/dy$. We introduce the dimensionless

parameter $\mu = fH'(y)/\beta H$ to characterize the steepness of the topography relative to that of the Coriolis frequency. As a result, inserting (10) into (8) and using $d/dy(f/H) = (\beta/H)(1 - \mu)$ yields

$$\frac{\partial \tilde{p}}{\partial t} - c\left(1 + \frac{\mu}{\mu - 1}\frac{H_1}{H_2}\right)\frac{\partial \tilde{p}}{\partial x} = \frac{g'H_2}{H}\left(1 + \frac{\mu}{\mu - 1}\frac{H_1}{H_2}\right)w_E, \qquad (11)$$

where $c = g'\beta H_1 H_2/f^2 H$. Equation (11) has exactly the same structure as the equation for the baroclinic mode in the flat-bottom case. The only difference is that both the phase speed and the forcing term are multiplied by the same factor $1 + \mu H_1/(\mu - 1)H_2$. We are interested here in the asymptotic behavior of Eq. (11) in the limit of a steep topography, that is the case $\mu \gg 1$. Formally, when μ increases indefinitely, this factor tends to $H/H_2 > 1$, and Eq. (11) tends to

$$\frac{\partial \tilde{p}}{\partial t} - \frac{g'\beta H_1}{f^2}\frac{\partial \tilde{p}}{\partial x} = g'w_E. \qquad (12)$$

For the particular situation of an x-independent Ekman pumping (hence also approximately with an x dependence on a scale large compared to the baroclinic wavelength), the baroclinic response in $\tilde{p}$ is amplified by the same factor H/H_2 since this factor multiplies the wind forcing. Furthermore, since the baroclinic contribution to p_1 is $-(H_2/H)\tilde{p}$ over a flat bottom [from Eq. (9)] while $p_1 \approx -\tilde{p}$ in a pressure compensated situation (as occurs for $\mu \gg 1$; see below), the ratio $|p_1/\tilde{p}|$ also is amplified by the factor H/H_2, and overall the Rossby wave sea-level response is amplified by the factor $(H/H_2)^2$ compared to the flat-bottom response. For small-scale x dependence in w_E, the possibility of resonances makes the degree of topographic amplification more dependent upon the particular situation.

For $H = H(y)$, Eq. (9) becomes

$$\frac{\partial}{\partial x}\left[\frac{d}{dy}\left(\frac{H}{f}\right)p_1 + \frac{d}{dy}\left(\frac{H_2}{f}\right)\tilde{p}\right] = -w_E. \qquad (13)$$

Integrating this equation over longitude yields the following relations:

$$p_1 = -\frac{H}{H_2}\frac{1 - \mu}{1 - H\mu/H_2}\tilde{p} + \frac{f^2}{\beta H}\frac{\displaystyle\int_{x_E}^{x} w_E \, dx' - F(y, t)}{1 - \mu} \qquad (14)$$

$$p_2 = \frac{1 - H/H_2}{1 - H\mu/H_2}\tilde{p} + \frac{f^2}{\beta H}\frac{\displaystyle\int_{x_E}^{x} w_E \, dx' - F(y, t)}{1 - \mu}, \qquad (15)$$

using $p_2 = p_1 + \tilde{p}$. Here $F(y, t)$ is the eastern boundary value for the quantity $(d/dy)(H/f)p_1 + (d/dy)(H_2/f)\tilde{p}$. For large μ, the asymptotic expressions for p_1 and p_2 become
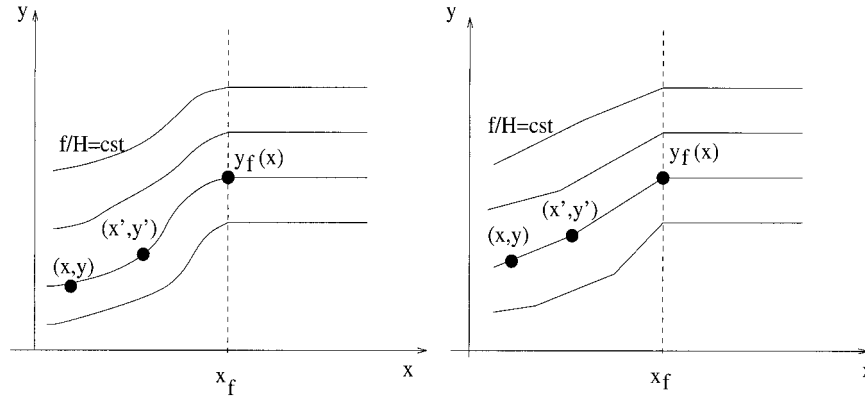
FIG. 2. Left panel: Smooth characteristics, f/H = const. Right panel: Same characteristics approximated by piecewise straight lines.

$$p_1 \sim -\tilde{p} + O\left(\frac{1}{\mu}\right) \qquad (16)$$

$$p_2 \sim -\frac{1}{\mu}\left[\frac{H_1}{H}\tilde{p} + \frac{f^2}{\beta H}\left(\int_{x_E}^{x} w_E\, dx' - F(y, t)\right)\right]. \qquad (17)$$

Equation (16) shows that the surface pressure is dominated by the contribution of the baroclinic pressure in this limit; thus, sea level is mostly indicative of baroclinic Rossby wave activity, with a lesser influence from barotropic motions. Equation (17) shows that the lower-layer pressure varies as the inverse of μ, indicative of pressure compensation.

b. Topography varying only with longitude

We now consider a topography varying with longitude only, which becomes flat eastward of the longitude $x = x_f < x_E$. The resulting barotropic characteristics, $\Pi \equiv f/H$ = const, are illustrated in Fig. 2 along with other notation. Sometimes, for analytic tractability, the continuous topographic contours are approximated as straight lines (right panel of Fig. 2). In this case Eq. (6) becomes

$$\Psi_x \Pi_y - \Psi_y \Pi_x = \text{curl}\left(\frac{\tau}{H}\right) + \frac{H_1}{H^2}J(\tilde{p}, H). \quad (18)$$

We integrate this along the characteristics, where the differential elements dx and dy are related by

$$\Pi_x\, dx + \Pi_y\, dy = 0. \qquad (19)$$

Multiplying (18) by dx and using (19) yields

$$\Pi_y(\Psi_x dx + \Psi_y dy) = \left[\text{curl}\left(\frac{\tau}{H}\right) + \frac{H_1}{H^2}J(\tilde{p}, H)\right]dx. \quad (20)$$

Since $\Pi_y = \beta/H$ and $H\,\text{curl}(\tau/H) = \text{curl}\tau - \tau_y H'(x)/H(x)$ when H varies only with longitude, Eq. (20) can be rewritten as

$$d\Psi = \frac{1}{\beta}\left[\text{curl}\tau - \frac{\tau_y H'(x)}{H} - \frac{H_1}{H}H'(x)\frac{\partial \tilde{p}}{\partial y}\right]dx. \quad (21)$$

We now integrate (21) between two points, (x, y) and (x_f, y_f), belonging to the same characteristic, where the latter point is taken at the boundary between the flat-bottom region and the region with topographic variations. The result is

$$\Psi(x, y) = \Psi(x_f, y_f(x)) + \int_{x_f}^{x} \frac{1}{\beta}\left[\text{curl}\tau - \frac{\tau_y H'}{H} - \frac{H_1}{H}H'\frac{\partial \tilde{p}}{\partial y}\right](x', y'(x'))\, dx'. \qquad (22)$$

Since the integration is performed along a characteristic, we have

$$\Pi(x, y) = \Pi(x', y') = \Pi(x_f, y_f) \qquad (23)$$

so that y' and y_f can be regarded as function of x. By differentiating (23) with respect to x, the following expressions for dy'/dx and dy_f/dx are obtained:

$$\frac{dy'}{dx} = -\mu(x, y)\frac{H(x')}{H(x)}, \qquad \frac{dy_f}{dx} = -\mu(x, y)\frac{H(x_f)}{H(x)}, \quad (24)$$

where μ is the dimensionless topographic steepness parameter defined by $\mu = fH'(x)/\beta H(x)$. By keeping in mind (24), as well as that $H(x')/f(y') = H(x)/f(y)$ along a characteristic, we can take the derivative of (22) with respect to x to obtain

$$\frac{\partial \Psi}{\partial x} = -\mu \frac{H(x_f)}{H(x)} \frac{\partial \Psi}{\partial y}(x_f, y_f) + \frac{1}{\beta}\left[\text{curl}\tau - \frac{\beta\mu\tau_y}{f} - \frac{\beta\mu H_1}{f}\frac{\partial \tilde{p}}{\partial y}\right]$$

$$- \frac{\mu(x, y)}{\beta H(x)} \int_{x_f}^{x} H(x')\frac{\partial}{\partial y}\left[\text{curl}\tau - \frac{\beta\mu\tau_y}{f} - \frac{\beta\mu H_1}{f}\frac{\partial \tilde{p}}{\partial y}\right](x', y') \, dx'. \tag{25}$$

We wish to express $\beta\partial_x\Psi - \text{curl}\tau$, which also appears in (8) in a way that distinguishes in (25) between the wind forcing and the baroclinic response functionally related to $\tilde{p}$. A provisional decomposition is

$$\beta\frac{\partial \Psi}{\partial x} - \text{curl}\tau = \mathcal{F} - \frac{\beta H_1}{f}L(\tilde{p}), \tag{26}$$

where $\mathcal{F}$ denotes "forcing" and $L(\tilde{p})$ denotes "functional of $\tilde{p}$," defined by

$$\mathcal{F} = -\frac{\mu\beta H(x_f)}{H(x)} \frac{\partial \Psi}{\partial y}(x_f, y_f) - \frac{\beta\mu\tau_y}{f}$$
$$- \frac{\mu}{H}\int_{x_f}^{x} H(x')\frac{\partial}{\partial y}\left[\text{curl}\tau - \frac{\beta\mu\tau_y}{f}\right](x', y') \, dx' \tag{27}$$

$$L(\tilde{p}) = \mu\left[\frac{\partial \tilde{p}}{\partial y} - \int_{x_f}^{x} \frac{\partial}{\partial y}\left(\mu\frac{\partial \tilde{p}}{\partial y}\right)(x', y'(x')) \, dx'\right]. \tag{28}$$

By inserting (26) into (8), a formal expression for the evolution equation of the baroclinic mode is obtained,

$$\frac{\partial \tilde{p}}{\partial t} - c\frac{\partial \tilde{p}}{\partial x} = \frac{g'H_2}{H}w_E - \frac{g'H_1}{fH}\left[\mathcal{F} - \frac{\beta H_1}{f}L(\tilde{p})\right]. \tag{29}$$

This is an integro–differential equation for $\tilde{p}$. The left side of this equation has the classical form for zonal propagation at the standard long Rossby wave speed, c, while the right side contains both local and nonlocal wind forcing and an unfamiliar integral operator, L. In some special cases below, we will show how $L(\tilde{p})$ contributes both to an enhancement of the propagation speed and to an energy exchange with the barotropic mode (see appendix D).

1) SOLUTION IN THE FLAT-BOTTOM REGION: $x_f \leq x \leq x_E$

In the eastern, flat-bottom region, Eqs. (6) and (7) reduce to

$$\beta\frac{\partial \Psi}{\partial x} = \text{curl}\tau \tag{30}$$

$$\frac{\partial \tilde{p}}{\partial t} - \frac{g'\beta H_1 H_2}{f^2 H}\frac{\partial \tilde{p}}{\partial x} = g'\frac{H_2}{H}w_E. \tag{31}$$

This set of equations is isomorphic to one by Frankignoul et al. (1997). The general solution here is given by

$$\Psi(x, y) = \frac{1}{\beta}\int_{x_E}^{x} \text{curl}\tau(x', y) \, dx' \tag{32}$$

$$\tilde{p}(x, y, t) = \tilde{p}(x_E, t^*)$$
$$+ \frac{g'H_2}{H}\int_{t^*}^{t} w_E(x + c(t - t'), y, t') \, dt', \tag{33}$$

where $t^*(x, t) = t + (x - x_E)/c$.

2) SOLUTION OVER A LINEAR SLOPE

To obtain explicit analytical results, we consider Eq. (29) in the case where the topography, $H(x)$, is a linear function of longitude (see the right side of Fig. 2) and the wind stress, $\tau(y, t)$, is independent of longitude. In this case, we show in appendix B that $\mathcal{F}$ takes the following form:

$$\mathcal{F} = \mu\left[-\frac{\beta H(x_f)}{H(x)}\frac{\partial \Psi}{\partial y}(x_f, y_f) + \frac{\beta}{f}\left(\tau_y(y^*) \ln\left(\frac{f(y)}{f(y^*)}\right) - \tau_y(y_f)\right)\right] + \frac{H(x_f)}{H(x)}\text{curl}\tau(y_f) - \text{curl}\tau(y)$$
$$+ \frac{\beta}{f}(\tau_x(y) - \tau_x(y_f)), \tag{34}$$

where y^* is such that $y \leq y^* \leq y_f$. As can be seen, $\mathcal{F}$ comprises two terms, one proportional to μ (i.e., increasing with topographic steepness) and one that is order unity (i.e., of the same order of magnitude as the baroclinic forcing in the flat-bottom case). Thus, over steep topography, $\mathcal{F}$ is dominated by the first term and can become arbitrarily large.

Given an arbitrary point (x_0, y_0) on the characteristic

joining (x, y) to (x_f, y_f), we show in appendix A how to perform a local analysis of the operator $L(\tilde{p})$ in terms of the following quantities:

$$\tilde{p}_\varepsilon(x, y) = \iint_{\mathcal{D}_\varepsilon(x_0, y_0)} \hat{p}(k, l) e^{i(kx + ly)} \, dk \, dl \quad (35)$$

$$\tilde{p}_T(x, y) = \iint_{\mathcal{D}_T(x_0, y_0)} \hat{p}(k, l) e^{i(kx + ly)} \, dk \, dl, \quad (36)$$

where $\hat{p}(k, l)$ is the Fourier spectrum of $\tilde{p}$ with longitudinal and latitudinal wavenumbers k and l respectively, $\mathcal{D}_\varepsilon(x_0, y_0)$ is the strip of the wavenumber space defined by $-\varepsilon \leq k + l\mu(x_0, y_0) \leq \varepsilon$ with $\varepsilon \ll 1$, and $\mathcal{D}_T(x_0, y_0)$ is the total wavenumber space minus $\mathcal{D}_\varepsilon(x_0, y_0)$. The domains $\mathcal{D}_\varepsilon(x_0, y_0)$ and $\mathcal{D}_T(x_0, y_0)$ form a partition of the total wavenumber space so that $\tilde{p} = \tilde{p}_\varepsilon + \tilde{p}_T$. Since the operator L is linear, it follows that

$$L(\tilde{p}) = L(\tilde{p}_\varepsilon) + L(\tilde{p}_T). \quad (37)$$

The asymptotic expressions of $L(\tilde{p}_\varepsilon)$ and $L(\tilde{p}_T)$ in the limit of large μ are shown in appendix A to be given by

$$L(\tilde{p}_T) = \frac{\partial \tilde{p}_T}{\partial x} + \left(\mu \frac{\partial \tilde{p}_T}{\partial y} - \frac{\partial \tilde{p}}{\partial x} \right)(x_f, y_f) \quad (38)$$

$$L(\tilde{p}_\varepsilon) = -\frac{\partial}{\partial x} \left((x - x_f) \frac{\partial \tilde{p}_\varepsilon}{\partial x} \right). \quad (39)$$

Two different regimes can thus be defined corresponding to the cases where $L(\tilde{p})$ is dominated either by $L(\tilde{p}_T)$ or $L(\tilde{p}_\epsilon)$ with the corresponding forms for Eq. (29) as follows:

Case $L(\tilde{p}_T) \gg L(\tilde{p}_\epsilon)$:

$$\frac{\partial \tilde{p}}{\partial t} - \frac{g' \beta H_1}{f^2} \frac{\partial \tilde{p}}{\partial x} = \frac{g' H_2}{H} w_E + \mathcal{F}^*,$$

$$\mathcal{F}^* = \mathcal{F} + \frac{g' H_1^2}{f^2 H} \left(\mu \frac{\partial}{\partial y} + \frac{\partial}{\partial x} \right) \tilde{p}(x_f, y_f). \quad (40)$$

$\tilde{p}$ locally parallel to f/H, $L(\tilde{p}_\epsilon) \gg L(\tilde{p}_T)$:

$$\frac{\partial \tilde{p}}{\partial t} - \frac{g' \beta H_1 H_2}{f^2 H} \frac{\partial \tilde{p}}{\partial x} = \mathcal{F}^{**} + \frac{g' \beta H_1^2}{f^2 H} \frac{\partial}{\partial x} \left((x_f - x) \frac{\partial \tilde{p}}{\partial x} \right),$$

$$\mathcal{F}^{**} = \mathcal{F} + \frac{g' H_2}{H} w_E. \quad (41)$$

For (x, y) close to (x_0, y_0), we have by construction $J(\tilde{p}_\epsilon, f/H) \approx 0$. In the case where $\tilde{p}_\epsilon$ is dominant, we shall have $J(\tilde{p}, f/H) \approx 0$ so that $\tilde{p}$ must appear locally parallel to the f/H contours, hence the denomination for the regime (41). On the other hand, note that it is not mathematically accurate to say that the first regime (40) should imply for $\tilde{p}$ to be locally nonparallel to the f/H contours. The reason is that there are some instances where $J(\tilde{p}_T, f/H)$ vanishes even if $\tilde{p}_T$ differs from zero,

for example, at a saddle point or a local extremum. This subtlety, however, should not be important in practice because such cases are generally very isolated.

Outside the two above regimes, the equation must be a linear combination of (41) and (40) in proportion to the contribution of $\tilde{p}_\epsilon$ and $\tilde{p}_T$ to the total sum $\tilde{p}$. In general, however, since the measure of $\mathcal{D}_\varepsilon$ tends toward zero as ε goes to zero, $\tilde{p}_\varepsilon$ should be close to zero if $\hat{p}(k, l)$ is finite over $\mathcal{D}_\varepsilon$, so the regime (40) should be the one most often encountered.

Equations (40) and (41) are one of the main theoretical results of this paper. In the main regime [i.e., Eq. (40)], as in the case of a topography varying in latitude only, there is an increase in phase speed by the factor H/H_2. The baroclinic forcing term, on the other hand, is much different since it increases with the topographic steepness to become much larger than over a flat bottom. This property is interpreted in the following sections as the means of creation of free baroclinic Rossby waves by an ocean ridge, which occurs through the conversion of energy from wind-driven barotropic motions. In contrast, in the second regime for which $\tilde{p}$ is locally parallel to f/H contours [i.e., Eq. (41)], a diffusion-like term occurs that does not exist in the flat-bottom case. The associated baroclinic energy dissipation is a result of conversion from the baroclinic to the barotropic mode.

Is there a phase speed enhancement associated with pressure compensation in this case? An explicit mathematical answer to this question—as for the topography varying only with latitude—could not be obtained. From our numerical solutions below, we learn that in some instances enhanced speed is observed, even where pressure compensation does not occur. This indicates that pressure compensation is actually not a necessary condition for enhanced propagation to occur, as is further discussed at the end of section 5.

4. Theory for the generation of Rossby waves by a ridge

According to the analyses above, steep topography ($\mu \gg 1$) affects the character of wind-forced, baroclinic Rossby waves in three main ways: it systematically enhances their phase speed by the ratio H/H_2, it introduces a dissipative term due to energy conversion to the barotropic mode where $\tilde{p}$ is aligned with f/H, and it increases the effectiveness of the wind forcing by $O(\mu)$ through energy conversion from the barotropic mode. Of these three effects, only the last is likely to be important in the generation and/or amplification of baroclinic Rossby waves by an ocean ridge. In this section, we investigate the dynamics of a simple model that attempts to describe how the third effect works. If we neglect the terms causing the phase speed amplification and the dissipation, Eq. (40) reduces to the simple forced-wave equation,

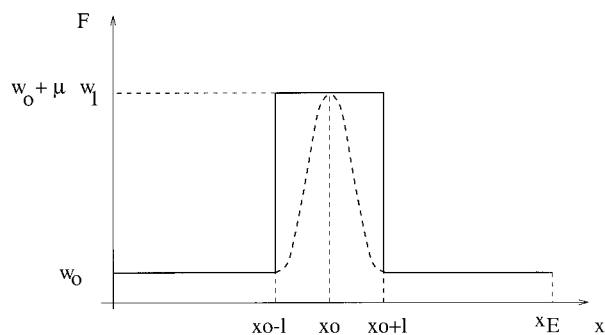$$\frac{\partial \tilde{p}}{\partial t} - c \frac{\partial \tilde{p}}{\partial x} = \mathcal{F}(x, t), \quad (42)$$

FIG. 3. Idealized forcing distributions: abrupt (solid line) and smooth (dashed line).

where the forcing term is $\mathcal{F} = g'H_2 w_E/H + \mathcal{F}^*$ with $\mathcal{F}^*$ from (40). As shown above, the latter is $O(\mu)$ times greater over a steep topography than over a flat bottom. To gain insight into the dynamics of (42), we replace $\mathcal{F}$ by idealized forms that match its qualitative character; specifically, we consider the following two types of "ridge forcing":

smooth forcing:

$$\mathcal{F}(x, t) = \begin{cases} w_0 \cos(\omega t), & |x - x_0| \geq l, \\ \left\{ w_0 + \frac{1}{2}\mu w_1 \left[1 + \cos\left(\frac{\pi(x - x_0)}{l}\right) \right] \right\} \cos(\omega t), & \\ & |x - x_0| < l. \end{cases}$$

(43)

abrupt forcing:

$$\mathcal{F}(x, t) = \begin{cases} w_0 \cos(\omega t), & |x - x_0| \geq l, \\ (w_0 + \mu w_1) \cos(\omega t), & |x - x_0| < l. \end{cases}$$ (44)

Figure 3 shows that these two functions are large over an interval of width $2l$ centered on x_0, representing the effect of the ridge.

The complete solution of (42) for the above forcing distributions is given in appendix C. For both types of forcing, free, baroclinic Rossby waves are generated west of the ridge, with an amplitude given by

$$A_{\text{smooth}} = -\frac{\mu w_1}{\omega} \frac{\sin(\pi k/k_T)}{(k/k_T)^2 - 1} \qquad (45)$$

$$A_{\text{abrupt}} = 2\frac{\mu w_1}{\omega} \sin(\pi k/k_T), \qquad (46)$$

where $k_T = \pi/l$ is an approximate wavenumber for the ridge and $k = \omega/c$ is the wavenumber of the Rossby waves. In each case the amplitude of the free waves generated by the ocean ridge is proportional to the amplitude of the ridge forcing, as well as its temporal period. The amplitude of the free waves generated also depends on the ratio of the wave wavelength to the width of the topographic region, or equivalently k/k_T, with the functional dependences shown in Fig. 4. There is a no-
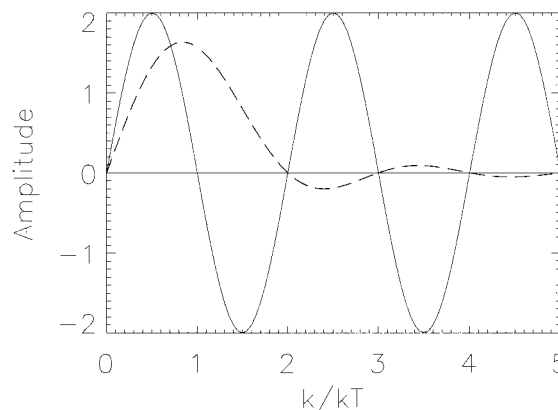

FIG. 4. Amplitude of the free baroclinic waves generated west of the idealized forcing distributions of Fig. 3 as a function of k/k_T: solid line is for the abrupt forcing; dashed line is for the smooth forcing.

table difference in the responses to the two types of forcing. For the smooth forcing, the amplitude function (45) has a global maximum at $k/k_T \approx 0.83$, vanishes for $k/k_T = 2$, and then becomes very small for values $k/k_T \geq 2$. Thus, free waves can be efficiently generated only if the width of the ridge forcing is comparable with the wavelength of the Rossby waves. On the other hand, free waves with maximum amplitude $2\mu w_1/\omega$ can be generated by abrupt ridge forcing even if the width of the ridge is not comparable with the wavelength, whenever k/k_T takes on the discrete values $n + \frac{1}{2}$, with n any integer. This limitation is not likely to be important in nature, however, since the frequency spectrum of the wind is broadband so that Rossby waves with wavelengths satisfying the required constraint should always exist.

5. Numerical solutions

a. Cases

Our previous analytical results are extended by three cases of idealized numerical solutions where the topography is a meridional midocean ridge of fixed longitudinal width but with several different heights, δH (Fig. 5). First, we investigate the propagation of a freely propagating baroclinic eddy initially east of the ridge, similar to Sakamoto and Yamagata (1997), to illustrate the enhancement of the phase speed over the ridge. Second, we consider the case of the baroclinic "wavemaker" that excites time-periodic motions at the eastern boundary (e.g., emission due to scattering by poleward-propagating coastal waves (Milliff and McWilliams 1994)): without additional forcing, baroclinic Rossby waves are strongly attenuated west of the ridge through coupling with the barotropic mode. In contrast, amplification is predicted for the same problem with WKB theory in Killworth and Blundell (1999). Third, baroclinic Rossby waves are forced by zonally uniform Ekman pumping to show that in this case it is possible for large-amplitude baroclinic
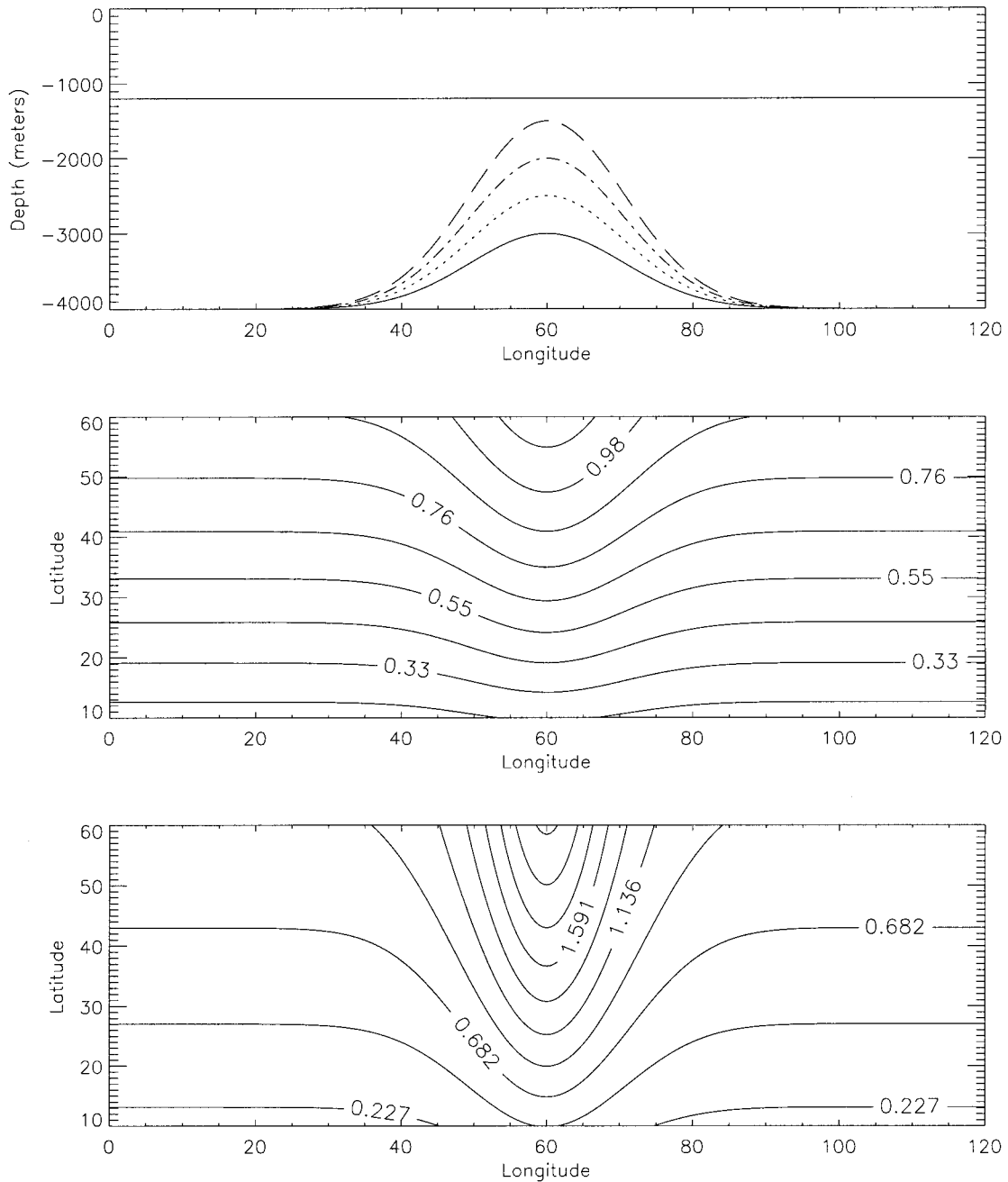
FIG. 5. Top: The idealized ridge for the four cases $\delta H = 1000$ m (solid), $\delta H = 1500$ m (dotted), $\delta H = 2000$ m (dotted–dashed), and $\delta H = 2500$ m (dashed). The horizontal solid line indicates the position of the layer interface. Middle: dimensionless contours $f/H = $ const for $\delta H = 1000$ m. Bottom: As above but for $\delta H = 2500$ m.

Rossby waves to be generated west of the ridge. In all cases we chose for the density stratification $\epsilon = (\rho_2 - \rho_1)/\rho_0 = 0.002$, $H_1 = 1200$ m, and $H_2 = 2800$ m (i.e., $H = 4000$ m) away from the ridge. The somehow unrealistic values for the ridge and stratification are dictated by the following considerations: 1) the ridge be wide enough for propagation features to be easily detected in longitude–time plots and 2) the amplification factor H/H_2

be important enough for the enhanced and flat-bottom phase speeds to be clearly distinct.

b. Numerical method

Numerical solutions are obtained by solving the following system of equations, equivalent to (6) plus (8), but somewhat simpler in form:

$$J\left(\frac{H}{f}, p_2\right) = \frac{g'\beta H_1}{f^2}\frac{\partial \eta_2}{\partial x} + w_E \qquad (47)$$

$$\frac{\partial \eta_2}{\partial t} - \frac{g'\beta H_1}{f^2}\frac{\partial \eta_2}{\partial x} = -\frac{\beta H_1}{f^2}\frac{\partial p_2}{\partial x} + w_E \qquad (48)$$

$$\eta_1 = \frac{p_2}{g} - \epsilon\eta_2. \qquad (49)$$

Equation (47) is obtained by taking the curl of the vertically integrated momentum equations divided by f; this allows us to use p_2 in place of Ψ. Equation (48) is Eq. (4), using the geostrophic approximation for $\mathbf{u}_2$ and a rewriting of Eq. (47) as follows:

$$J\left(\frac{H_2}{f}, p_2\right) = \frac{g'\beta H_1}{f^2}\frac{\partial \eta_2}{\partial x} - \frac{\beta H_1}{f^2}\frac{\partial p_2}{\partial x} + w_E. \qquad (50)$$

Equation (48) makes it clear that baroclinic Rossby waves propagate faster than the flat-bottom speed when pressure compensation occurs, that is, when p_2 vanishes. The energy equation corresponding for this system is shown in appendix D to be

$$\frac{\partial}{\partial t}\frac{\eta_2^2}{2} - \text{div}\mathcal{F}_E = p_1 w_E, \qquad (51)$$

where

$$\mathcal{F}_E = \frac{\beta}{f^2}\frac{H_1 p_1^2}{2}\hat{\mathbf{x}} + \frac{p_2^2}{2}\hat{\mathbf{z}} \times \boldsymbol{\nabla}\frac{H_2}{f}. \qquad (52)$$

The energy flux $\mathcal{F}_E$ at the boundary determines where the energy enters and leaves the domain. Because the flux is sign-definite with respect to the p_i, we can deduce the necessary boundary information: with respect to the first term on eastern and western boundaries, the former site is an energy source (where p_1 must be specified) and the latter a sink (where p_1 is freely evolving); with respect to the second term, p_2 must be specified where there is an energy source, namely, where ($\hat{\mathbf{z}} \times \boldsymbol{\nabla}H_2/f) \cdot \hat{\mathbf{n}} > 0$ with $\hat{\mathbf{n}}$ the outward normal direction.

For all cases the numerical domain is 120° wide in longitude and 50° wide in latitude with the southern boundary at 10°N. Thus, our boundary conditions are p_1 and p_2 specified at the eastern boundary and $p_2 = 0$ (i.e., no energy flux) where its value is required on the northern and southern boundaries. For time integrations we use second-order, centered finite difference operators, with a spatial resolution of 200 points in longitude × 800 points in latitude (in order to resolve the characteristics accurately and limit erroneous numerical dispersion when the ridge is steep). A spatially implicit scheme is used to integrate (47) for p_2, and a Runge–Kutta scheme is used to step (48) for η_2 forward in time, with a time step $\Delta t = 1.25 \times 10^4$ s.

An alternative numerical method is used for the periodic steady states in the wavemaker and wind-forced cases, where the solutions are sought with the form

$$p_2 = \hat{p}_2 e^{i\omega t}, \qquad \eta_2 = \hat{\eta}_2 e^{i\omega t}, \qquad \eta_1 = \hat{\eta}_1 e^{i\omega t}$$

so that Eqs. (47) and (48) become

$$J\left(\frac{H}{f}, \hat{p}_2\right) = \frac{g'\beta H_1}{f^2}\frac{\partial \hat{\eta}_2}{\partial x} + \hat{w}_E \qquad (53)$$

$$i\omega\hat{\eta}_2 - \frac{g'\beta H_1}{f^2}\frac{\partial \hat{\eta}_2}{\partial x} = -\frac{\beta H_1}{f^2}\frac{\partial \hat{p}_2}{\partial x} + \hat{w}_E. \qquad (54)$$

Equations (53) and (54) constitute a coupled system for $\hat{p}_2$ and $\hat{\eta}_2$ that involves complex coefficients and spatial variations only. An equation for $\hat{p}_2$ alone can be obtained by integrating (54) in longitude, which yields $\hat{\eta}_2$ in terms of $\hat{p}_2$:

$$\hat{\eta}_2 = \frac{1}{g'}\left[\hat{p}_2 + \frac{i\mathcal{F}}{\omega} - ik_1\mathcal{P}\right], \qquad (55)$$

where $\mathcal{F}$ and $\mathcal{P}$ are defined by

$$\mathcal{P}(x, y) = e^{ik_1x}\int_x^{x_E} e^{-ik_1x'}\hat{p}_2(x', y) \, dx' \qquad (56)$$

$$\mathcal{F}(x, y) = i\omega\left(g\hat{\eta}_1(x_E, y)e^{ik_1(x-x_E)}\right.$$
$$\left. - \frac{g'}{c_1}e^{ik_1x}\int_x^{x_E}\hat{w}_E(x', y)e^{-ik_1x'} \, dx'\right), \qquad (57)$$

with $c_1 = g'\beta H_1/f^2$ and $k_1 = \omega/c_1$. Inserting (55) into (53) then yields

$$i\omega\hat{p}_2 - g'J\left(\frac{H_2}{f}, \hat{p}_2\right) + \frac{\omega^2}{c_1}\mathcal{P} = \mathcal{F}. \qquad (58)$$

The latter is a first-order differential equation along the curves $H_2/f = $ const, which is solved numerically by a method of characteristics using spline interpolation under tension (using the FITPACK package with a tension parameter value of unity). Once $\hat{p}_2$ is obtained, $\hat{\eta}_2$ and $\hat{\eta}_1$ are diagnosed from (55) and (49). In both types of calculations a high spatial resolution of 3600 points in longitude and 400 points in latitude is used to avoid noise near steep slopes at high latitudes.

c. Results

1) FREELY PROPAGATING BAROCLINIC EDDY

In this case an initial Gaussian eddy propagates over a ridge located at the center of the computational domain. Figure 6 shows sea level and interface height at several times for the case $\delta H = 1000$ m. Figure 7 is the same but for the case $\delta H = 2500$ m. In general, the eddy shape appears to be less distorted by the steeper topography in the second case, where apart from signals propagating meridionally along the flanks of the ridge, the primary pattern change is a zonal elongation due to the Rossby wave speed decreasing with latitude $\propto\beta/f_2$ (as also occurs with a flat bottom). This is an indication that the system becomes less dispersive as the steepness
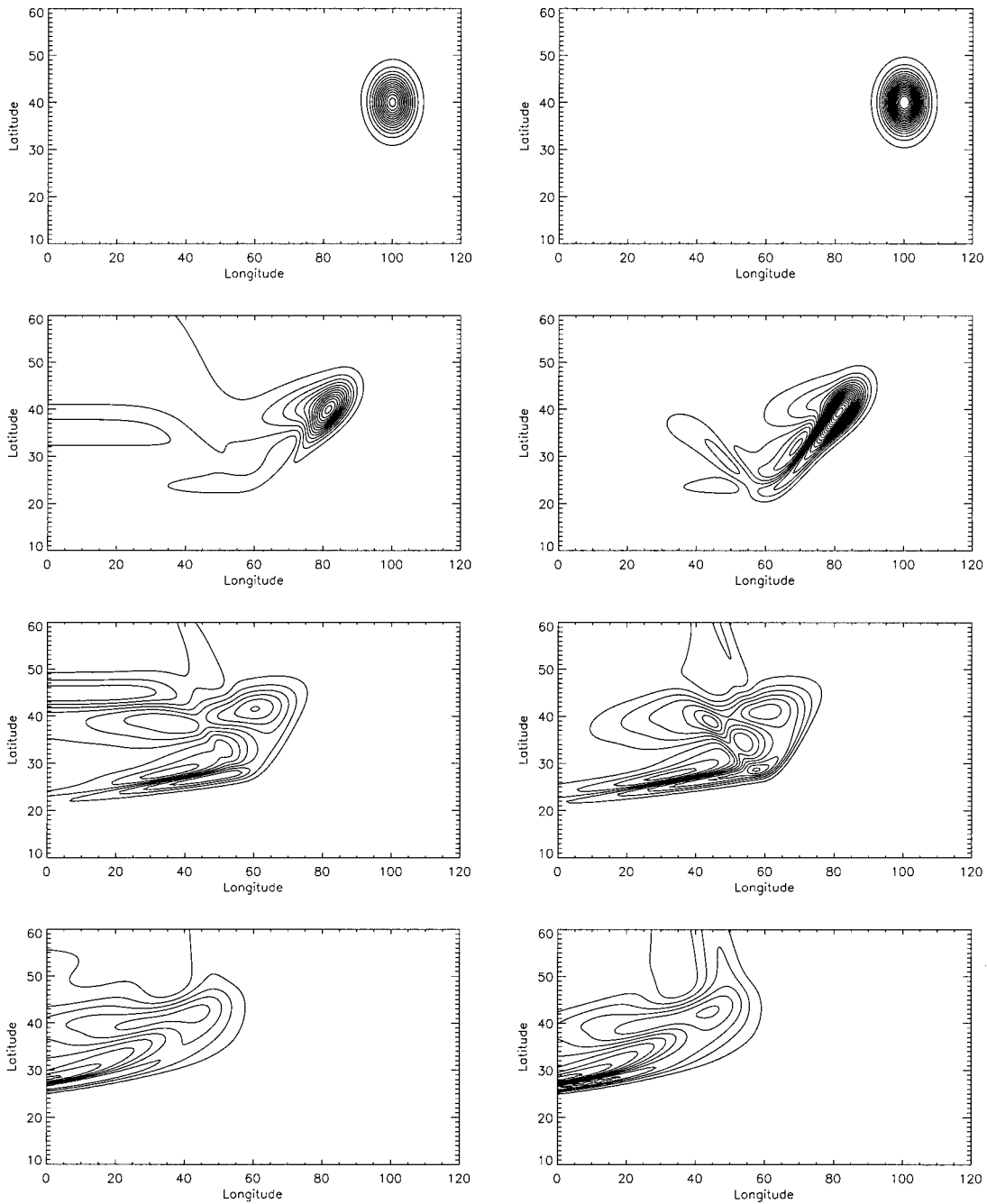
FIG. 6. Instantaneous values of the sea level (left panel) and layer interface (right panel) for the times $t = 0$, $t = 578$, $t = 1157$, and $t = 1735$ (in days), from top to bottom, in the free propagating eddy experiment with $\delta H = 1000$ m.

of the topography increases. We examine the propagation with Hovmöller diagrams (i.e., longitude–time plots) in Figs. 8 and 9 for an eddy core at latitude 40°N. For comparison we also draw a solid line to represent the flat-bottom speed, $c = g'\beta H_1 H_2/f^2 H$, and a dashed line to represent propagation enhanced by the factor H/H_2 discussed above. The speed enhancement in the case with $\delta H = 1000$ m is modest, but with $\delta H = 2500$ m it is substantial and close to the predicted factor, H/H_2, over a wide longitude band. Again, dispersive effects appear weaker with the steeper topography, where the spread of η_i contours is much smaller west of the ridge.

Figure 10 displays the temporal decay of baroclinic energy, $\iint \frac{1}{2}\eta_2^2$, as the eddy propagates across the basin. There is no energy decay until the eddy reaches the
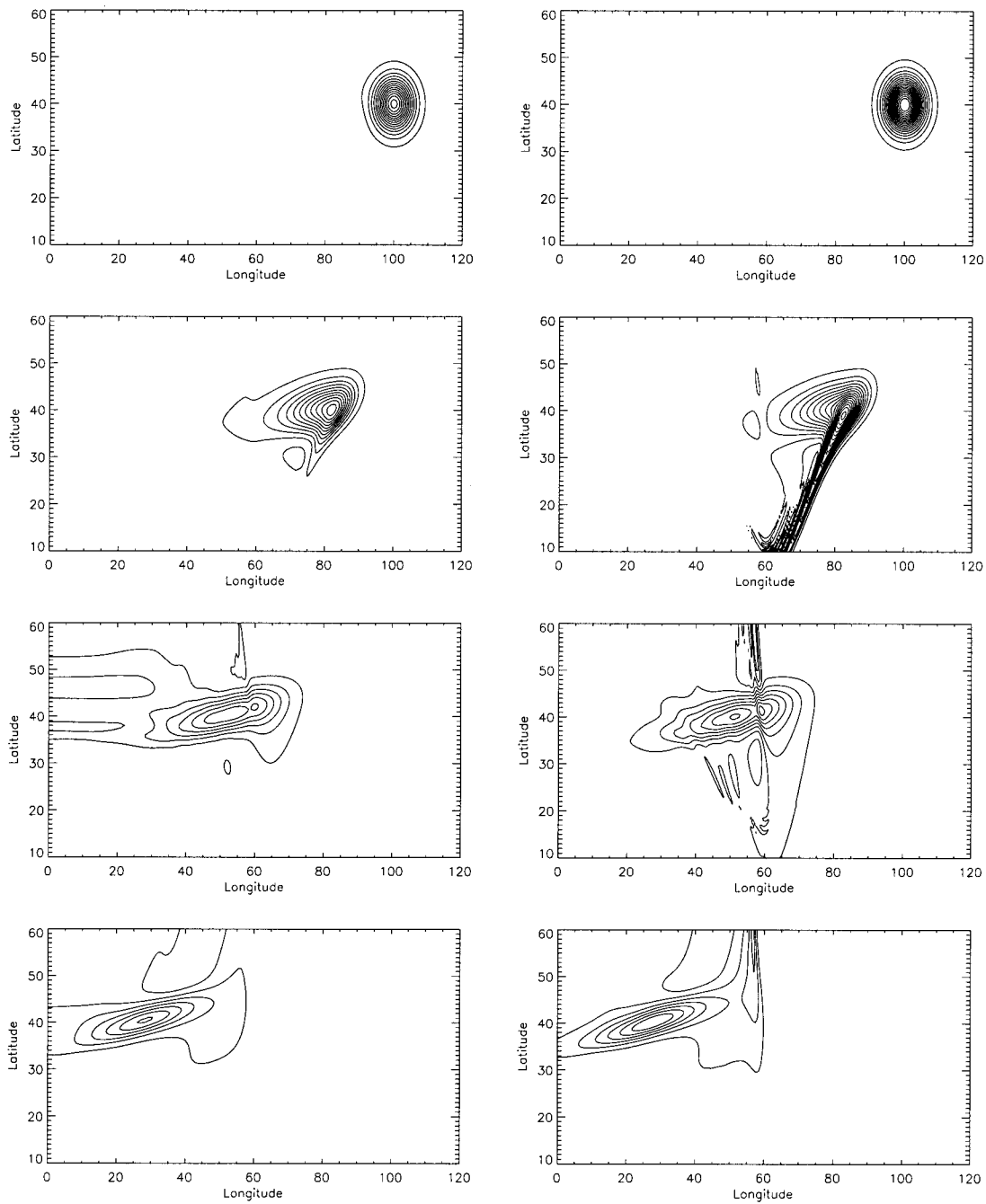
FIG. 7. As in Fig. 6 but with $\delta H = 2500$ m.

ridge and it decreases thereafter. It is greater overall in the case with steeper topography, even though the dispersive effects are weaker. The decay rate is shown in Fig. 11, where two different calculation methods are used as a check on the accuracy of our numerical model. The decay rate is largest at the time the eddy starts to cross the ridge. The two calculation methods give curves that are almost coincident in each case. The largest error occurs with the steeper topography; it is everywhere

less than 10% in magnitude, and its shape indicates it is primarily associated with the timing of the maximum dissipation.

2) EASTERN WAVEMAKER

In this case baroclinic Rossby waves are created at the eastern boundary by imposing equal oscillations in
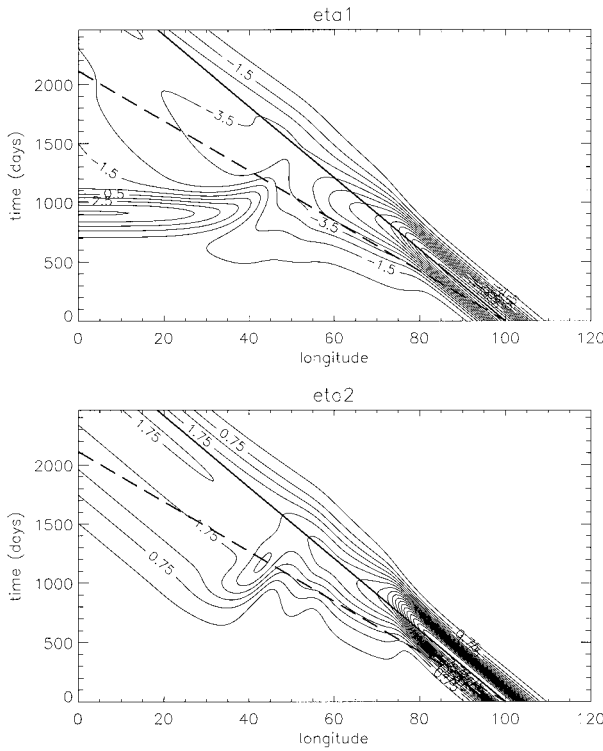
FIG. 8. Hovmöller diagrams at 40°N latitude for the sea level (top) and layer interface (bottom) in the free propagating eddy experiment with $\delta H = 1000$ m. Superimposed are straight lines for the standard phase speed (solid) and elevated phase speed $c_1 = g'\beta H_1/f^2$ discussed in the text (dashed).

FIG. 9. As in Fig. 8 but with $\delta H = 2500$ m.

η_1 and $-\eta_2(\epsilon H_2/H)$ at an annual frequency, $\omega = 2\pi/T$, $T = 1$ yr, and with a sinusoidal shape in latitude,

$$\hat{\eta}_2(x_E, y) = A \sin\left(\frac{\pi(y - y_S)}{D}\right),$$

$$\hat{\eta}_1(x_E, y) = -\epsilon\frac{H_2}{H}\hat{\eta}_2,$$

where y_S is the latitude of the southern boundary and D the latitudinal extent of the basin; this forcing creates no barotropic energy there. We choose $A = 10$ m. Also, no forcing is imposed in the interior, so the only source of energy is at the eastern boundary. We set $\hat{w}_E = 0$. For comparison, the solutions for $\hat{\eta}_1$ and $\hat{\eta}_2$ in the flat-bottom case are

$$\hat{\eta}_2 = A \sin\left(\frac{\pi(y - y_S)}{D}\right)e^{ik(x-x_E)} \tag{59}$$

$$\hat{\eta}_1 = -\epsilon\frac{H_2 A}{H} \sin\left(\frac{\pi(y - y_S)}{D}\right)e^{ik(x-x_E)}. \tag{60}$$

These solutions comprise solely freely propagating baroclinic Rossby waves with zonal wavenumber $k = \omega/c$; for each quantity the root-mean-square variability,
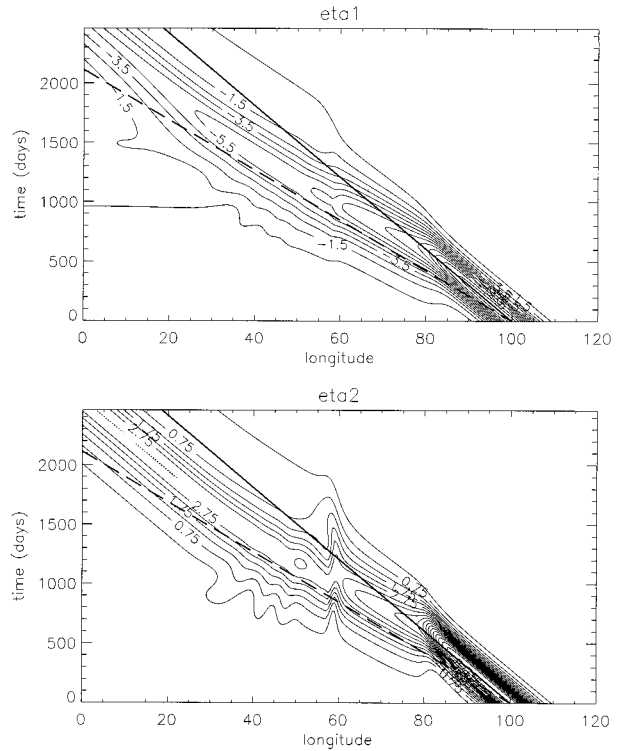
$$\mathrm{rms}\,\eta_1 = \left(\frac{1}{T}\int_0^T \frac{\eta_1^2}{2}\,dt\right)^{1/2} = \frac{1}{2}|\hat{\eta}_1|,$$

$$\mathrm{rms}\,\eta_2\left(\frac{1}{T}\int_0^T \frac{\eta_2^2}{2}\,dt\right)^{1/2} = \frac{1}{2}|\hat{\eta}_2|, \tag{61}$$

is longitudinally uniform at each latitude. The effect of the ridge on these two quantities is illustrated in Figs. 12, 13, 14, and 15, which display $|\hat{\eta}_1|$ (top) and $|\hat{\eta}_2|$ in the cases $\delta H = 1000$ m, $\delta H = 1500$ m, $\delta H = 2000$ m,
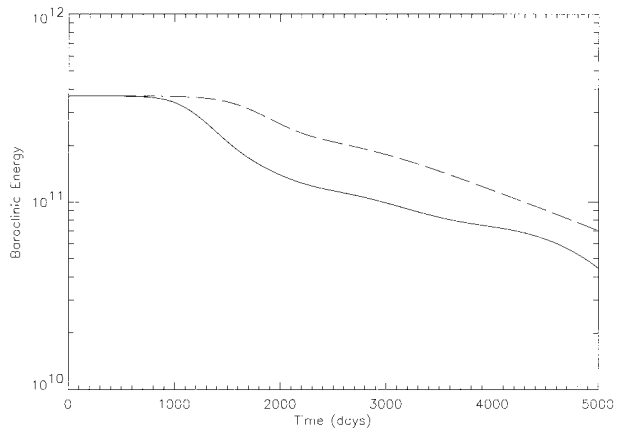

FIG. 10. Temporal decay of the baroclinic energy (basin integral of η_2^2) in the free propagating eddy experiments for $\delta H = 1000$ m (dashed line) and $\delta H = 2500$ m (solid line).
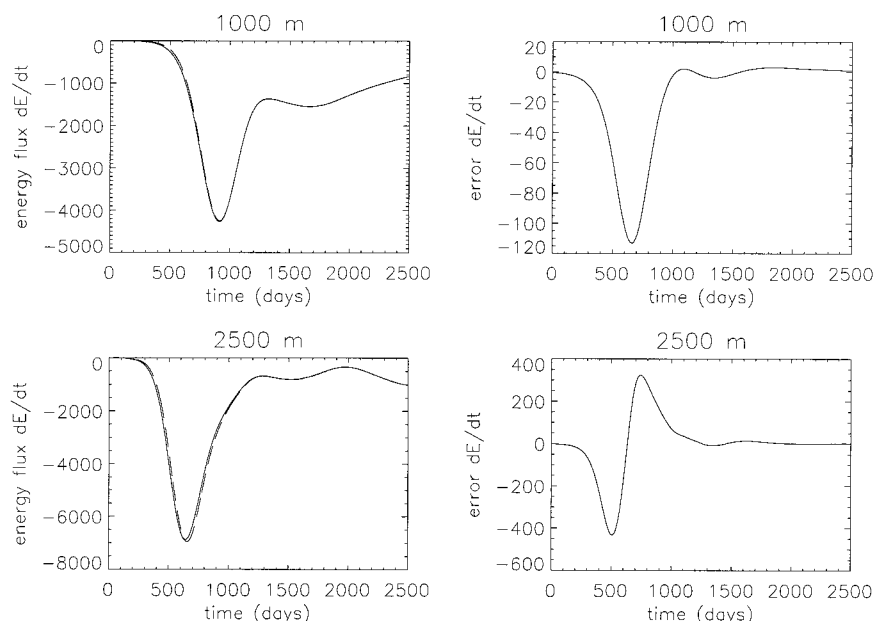
FIG. 11. Left panel: Energy fluxes dE/dt estimated from the curves depicted in Fig. 10 (dashed line) superimposed with those estimated from the flux formula given in appendix D (soline line). Right panel: The difference between the two curves, which gives an indication of the spurious numerical energy sources and sinks.

and $\delta H = 2500$ m, respectively. In each figure the eastern part of the domain is flat, so the solutions are the same as described above. In the steeper case (Fig. 15), the coupling along the f/H contours is quite strong, so most of the baroclinic energy is converted to barotropic energy that then propagates out of the domain to the south. As a result, the amount of baroclinic energy present in the western part of the domain is quite small; this behavior is also evident in the sea level. With a less steep ridge (Fig. 14), less energy is lost through the southern boundary because the f/H contours are then more zonally aligned. As a result, barotropic energy is seen to appear in the northwestern part of the domain in the sea level, suggesting that it was provided by conversion of baroclinic energy from the northeastern part of the domain. Although the amount of baroclinic energy in the western part has somewhat increased in comparison to the previous case, it still remains considerably reduced in comparison to its level in the eastern part. As the ridge height further decreases, Figs. 12 and 13, the sea level variability in the western part of the domain increases much more rapidly than the interface (i.e., baroclinic) variability. Indeed, in some locations, the variability of the sea level west of the ridge has become of the same order of magnitude, sometimes even larger, than in the eastern part of the domain, whereas the baroclinic variability is uniformly much lower than in the east. These results demonstrate clearly that the coupling with the barotropic mode cannot be neglected.

3) WIND FORCING

In this case wind-forced baroclinic Rossby waves are excited by an idealized Ekman pumping distribution,

$$\hat{w}_E(y) = w_0 \sin[\pi(y - y_S)/D], \qquad (62)$$

with same notation as above; we choose $w_0 = 10^{-6}$ m s^{-1}. For comparison, the solutions for $\hat{\eta}_1$ and $\hat{\eta}_2$ in the flat-bottom case are

$$\hat{\eta}_1 = -i\epsilon\left(\frac{H_2}{H}\right)^2 \frac{\hat{w}_E(y)}{\omega}(e^{ik(x-x_E)} - 1) \qquad (63)$$

$$+ \frac{f^2 \hat{w}_E}{g\beta H}(x - x_E)$$

$$\hat{\eta}_2 = \frac{iH_2}{H} \frac{\hat{w}_E(y)}{\omega}(e^{ik(x-x_E)} - 1). \qquad (64)$$

The baroclinic mode (i.e., the interface) has a free wave plus a forced response. In contrast, the sea level also possesses a term increasing with longitude from the eastern boundary that represents the Sverdrup balance for the barotropic mode. We display our results in the same form as for the wavemaker case in Figs. 16, 17, 18, and 19. In these cases, the presence of forcing makes a clear difference with the wavemaker case. In all figures, the baroclinic mode is stronger west of the ridge, with its amplitude increasing with the ridge height, in agreement with our theoretical prediction. The only exception occurs for the steeper topography, that is,
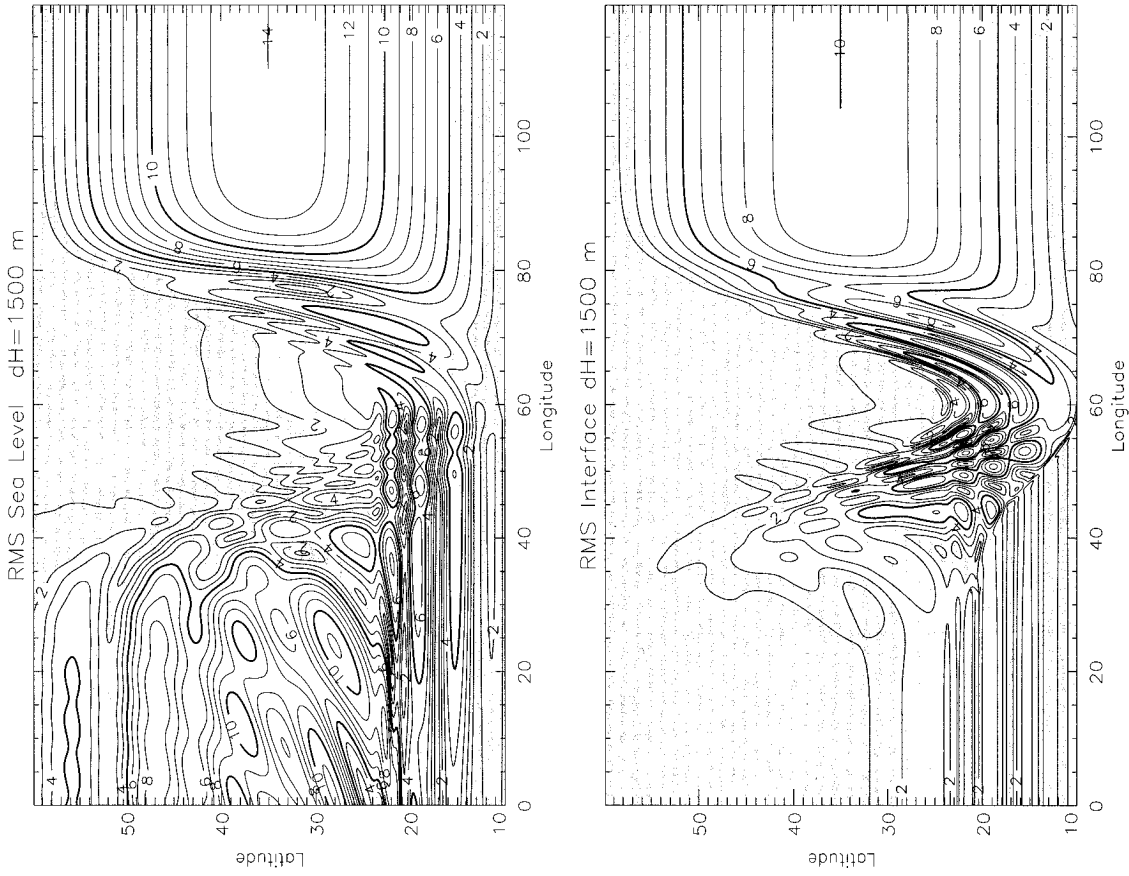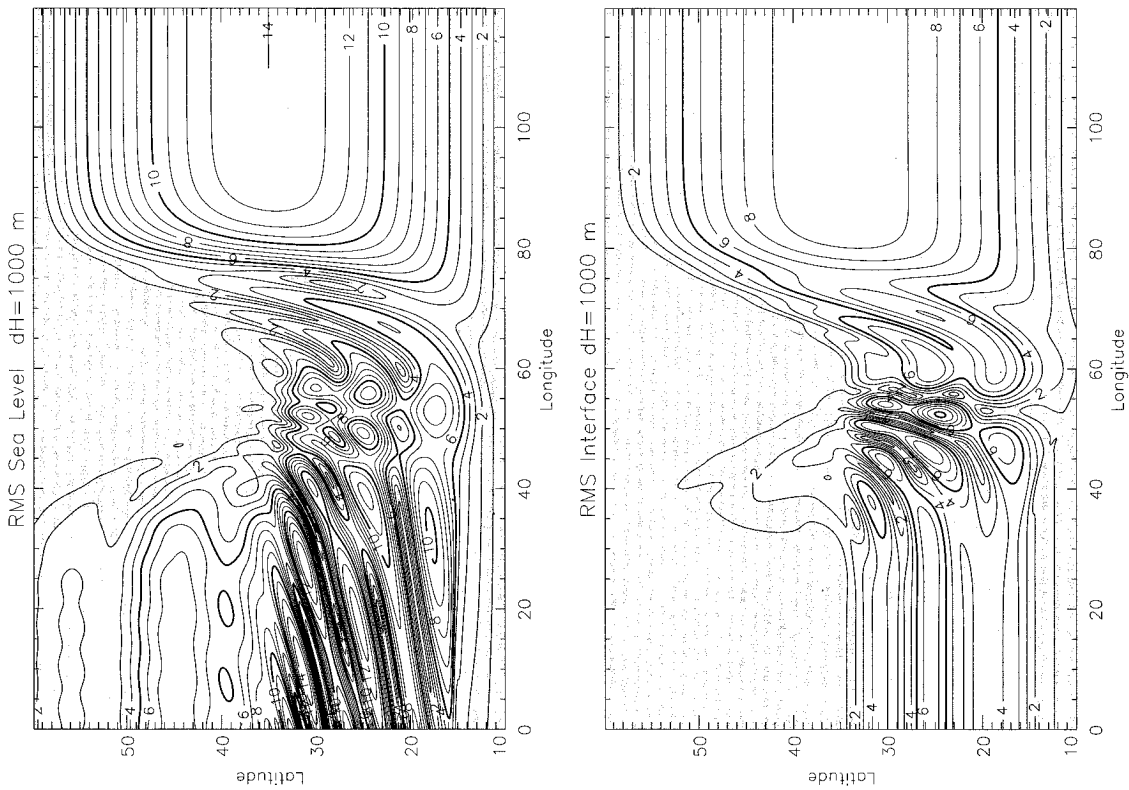
FIG. 12. Root-mean-square time variability of the sea level (top) and layer interface (bottom) in the wavemaker experiment with $\delta H = 1000$. Units are in millimeters for the sea level and meters for the layer interface.
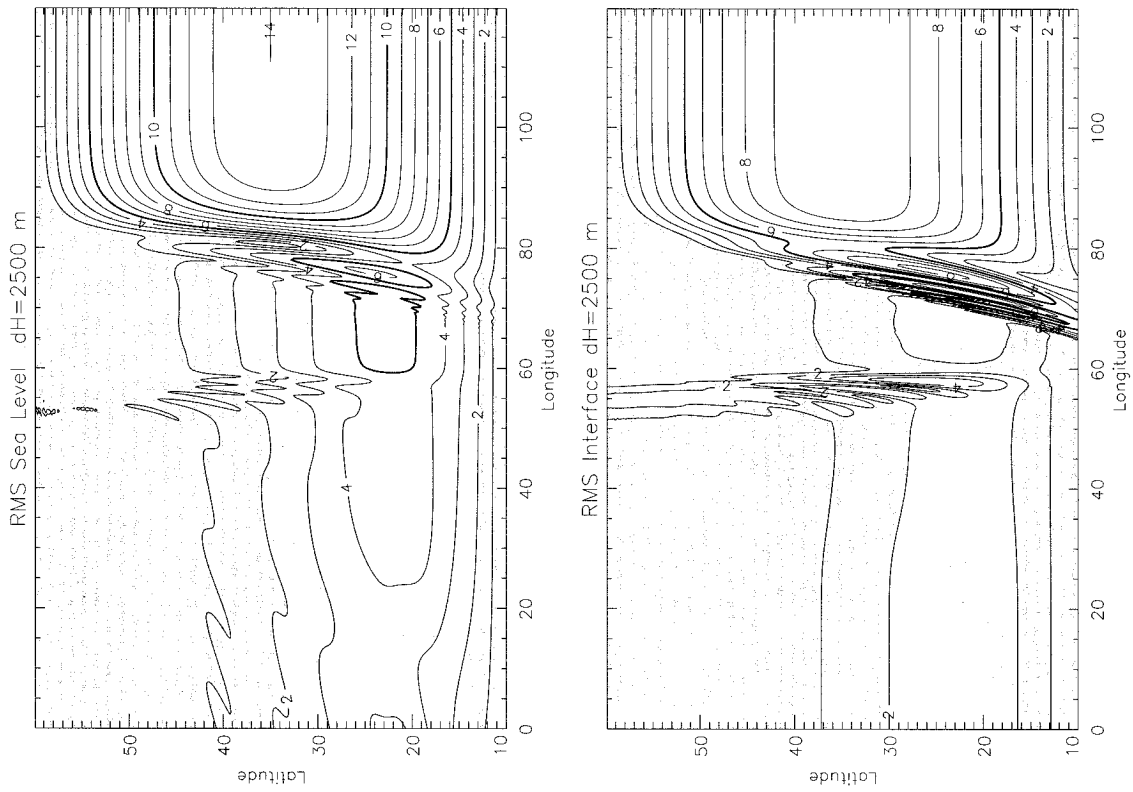
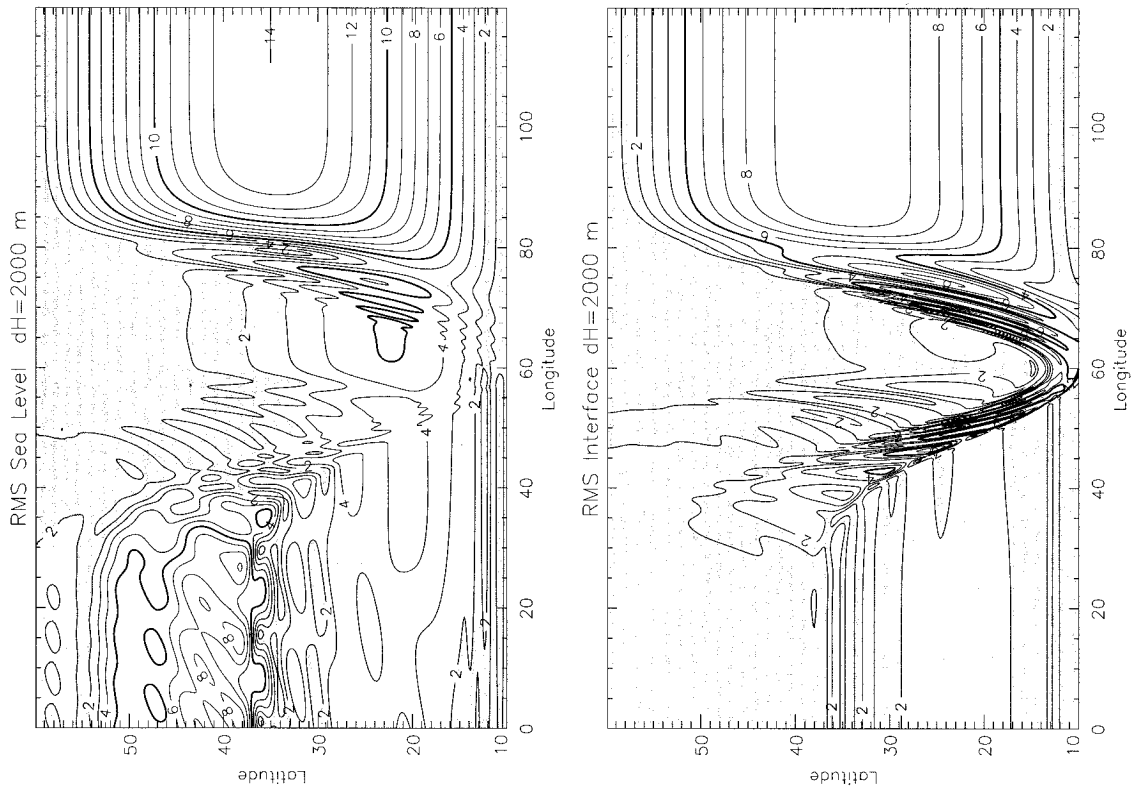FIG. 13. As in Fig. 12 but for $\delta H = 1500$ m.

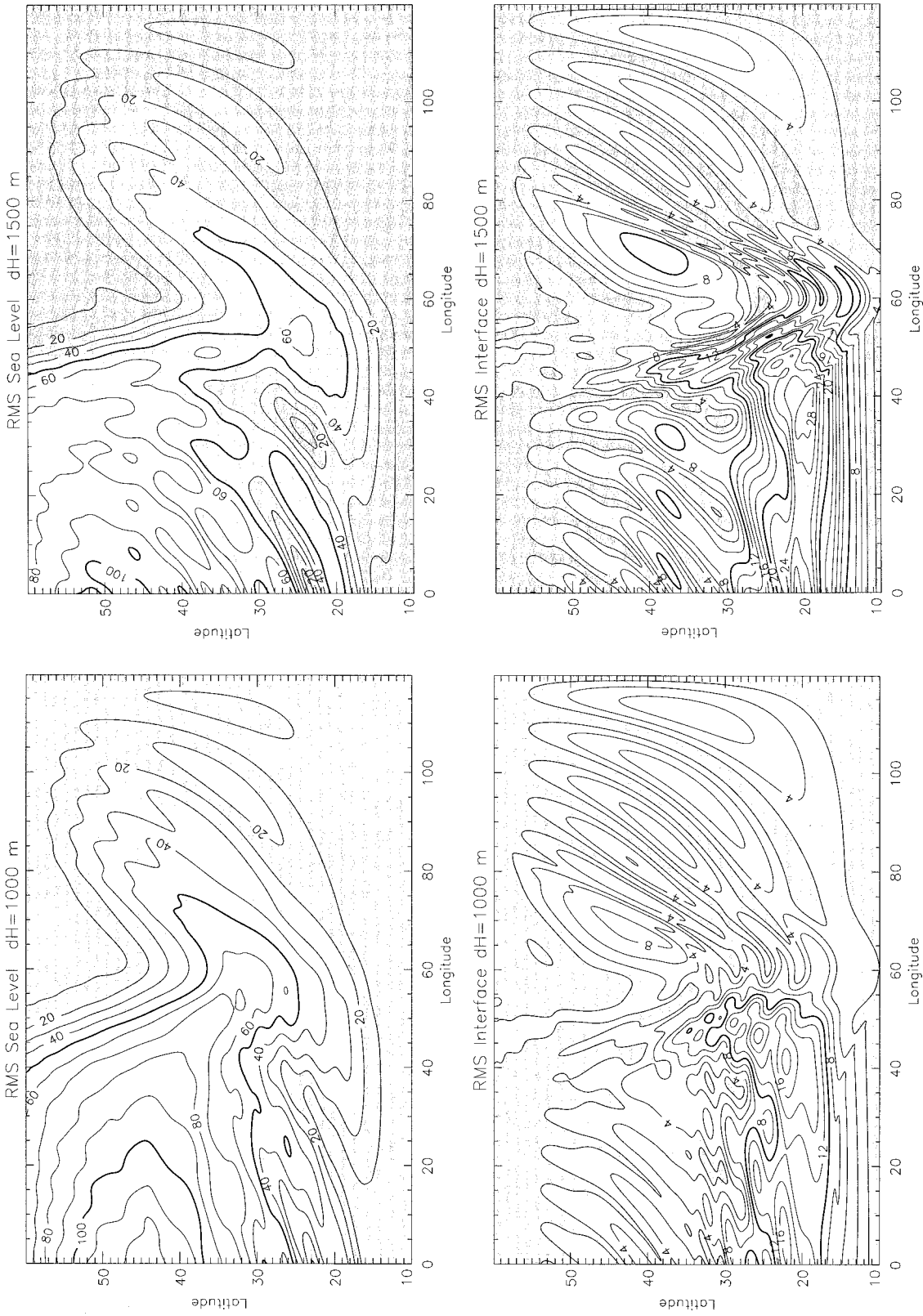FIG. 15. As in Fig. 12 but for $\delta H = 2500$ m.

FIG. 14. As in Fig. 12 but for $\delta H = 2000$ m.

FIG. 16. Root-mean-square time variability of the sea level (top) and layer interface (bottom) in the wind forced experiment with $\delta H = 1000$ m. Units are millimeters for the sea level and meters for the layer interface.
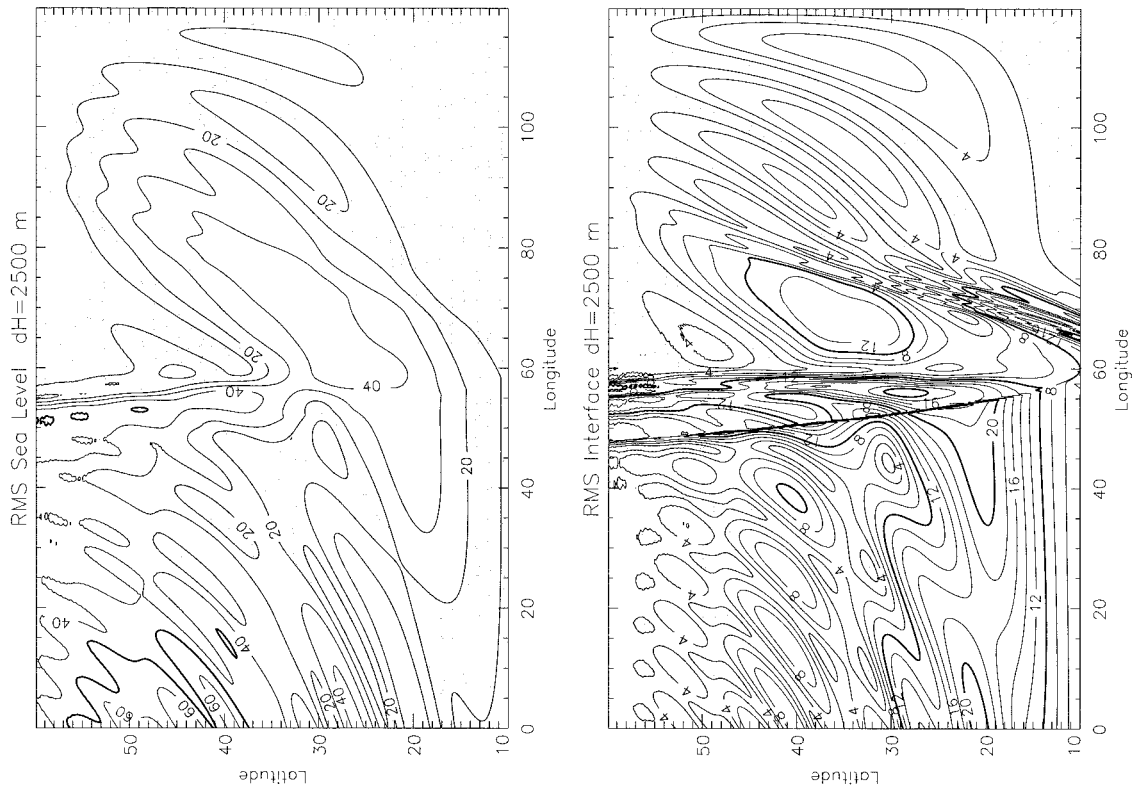
FIG. 17. As in Fig. 16 but for $\delta H = 1500$ m.

RMS Sea Level dH=2500 m

RMS Interface dH=2500 m

FIG. 19. As in Fig. 16 but for $\delta H = 2500$ m.

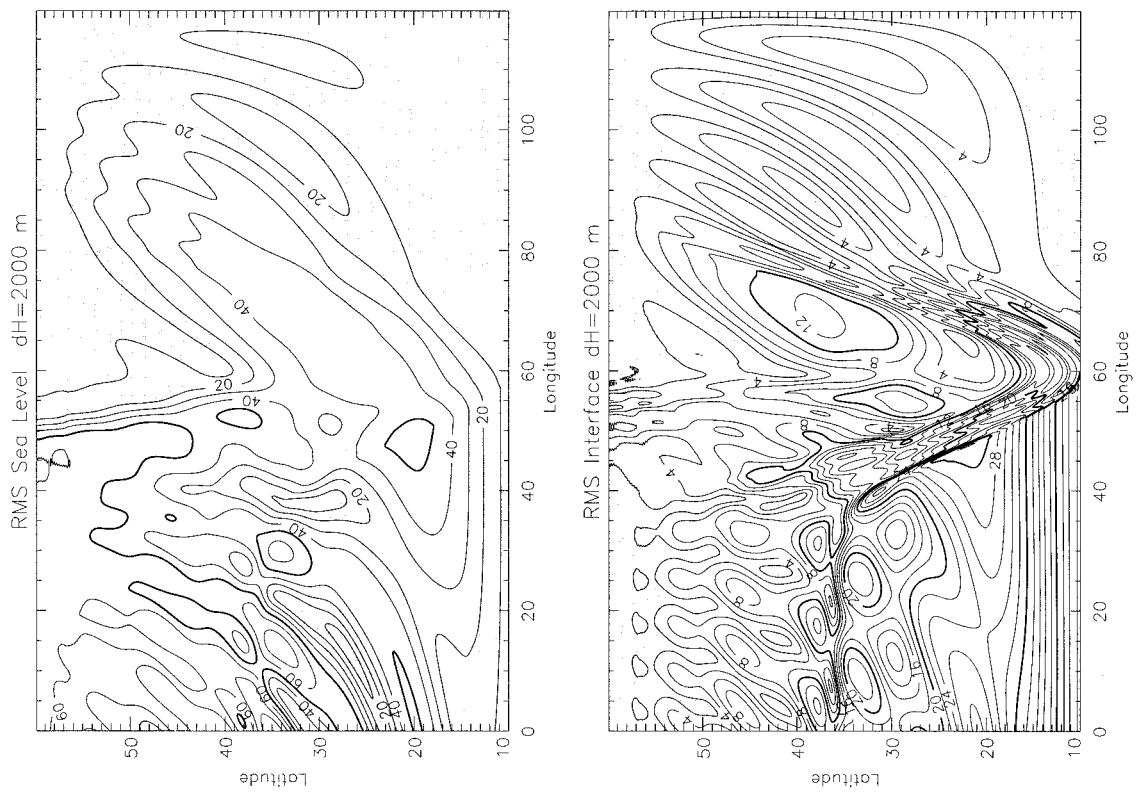RMS Sea Level dH=2000 m

RMS Interface dH=2000 m

FIG. 18. As in Fig. 16 but for $\delta H = 2000$ m.

$\delta H = 2500$ m, but in this case a significant amount of energy leaves the domain along strongly nonzonal characteristics (cf. the wavemaker case). In general, the largest baroclinic energy occurs in the southwestern part of the domain (as also occurs in the wavemaker case for the baroclinic waves that cross the ridge). The maximum value of the baroclinic mode in the eastern part of the domain is 7 m, while in the west it can reach values as high as 30 m in the $\delta H = 2000$ m solution, with typical values well above 10 m. These results demonstrate that wind forcing is associated with the creation of baroclinic energy west of the ridge, in agreement with our theoretical prediction.

d. Enhanced propagation speed and baroclinic compensation

Is enhanced propagation speed also present in the forced solutions? To answer this question, we analyze longitude–time plots of $\partial_x \eta_2$ every one degree in latitude for the steep topographic case $\delta H = 2000$ m [the zonal derivative is used to filter out the zonally independent component that is part of the directly forced response (White 1977)]. Two main regimes arise over the ridge (Fig. 20, right panel): an ill-defined propagation south of 30°N approximately, and a well-defined, enhanced propagation speed north of 30°N. As seen in Fig. 21, the first regime is achieved for values of the steepness parameter μ below or around unity, while the second regime is achieved for values of μ greater than unity. From the theoretical considerations in the introduction, we might expect that pressure compensation would be found in the northern part of the domain, but actually it is not. To understand this behavior, let us recall the equation for the baroclinic mode (48), which is valid over topography as well as over a flat-bottom. The way it is written suggests free waves with a phase speed of $g' \beta H_1 / f^2$, but actually this depends on whether $\partial_x p_2$ is correlated to $\partial_x \eta_2$. In the flat-bottom case, for instance, the two quantities are related by

$$\frac{\partial p_2}{\partial x} = \frac{g' H_1}{H} \frac{\partial \eta_2}{\partial x} + \frac{f^2 w_E}{\beta H} \tag{65}$$

so that the actual phase speed for η_2 is $g' \beta H_1 H_2 / f^2 H$. For a zonally uniform Ekman pumping, such a dependency would result in a straight line in a plot showing $\partial_x p_2$ versus $\partial_x \eta_2$. Such a plot is Fig. 22 for the same cases depicted in Fig. 20. In the southern part of the domain, $\partial_x p_2$ unexpectedly is strongly correlated to $\partial_x \eta_2$ with the approximate dependence

$$\frac{\partial p_2}{\partial x} \approx g' \frac{\partial \eta_2}{\partial x} + \cdots. \tag{66}$$

For such a dependence, the terms proportional to $\partial_x \eta_2$ and $\partial_x p_2$ in Eq. (48) approximately cancel each other so that the resulting equation is no longer a wave equation, explaining why propagation is not apparent in the

southern part of the basin. This seemingly well-defined correlation for the regime $\mu = O(1)$ is as yet unexplained. This correlation between $\partial_x p_2$ and $\partial_x \eta_2$ decreases as the latitude increases, as indicated by the seemingly random pattern in Fig. 22 (the three bottom panels). Propagation becomes well defined, and the phase speed is close to $g' \beta H_1 / f^2$. From this example, we conclude that the general condition for enhanced propagation speed is not pressure compensation (i.e., $p_2 \approx 0$) but a lack of correlation between $\partial_x p_2$ and $\partial_x \eta_2$.

e. Barotropic–baroclinic coupling

In the equation for the baroclinic mode (7), the coupling term with the barotropic mode is $H_1 / H^2 J(H, \Psi)$. In order to gain further insight into the coupling of the two modes, we seek to understand when the latter term acts as a source or sink of energy for the baroclinic mode. After multiplying Eq. (7) by η_2, a baroclinic energy equation is obtained in which this term implies a possible energy conversion:

$$\frac{1}{2} \frac{\partial \eta_2^2}{\partial t} = -g' J\left(\frac{\eta_2^2}{2}, \frac{H_1 H_2}{fH}\right) + \eta_2 \, \mathrm{curl}\left(\frac{H_2 \tau}{fH}\right)$$
$$+ \frac{H_1}{H^2} \eta_2 J(H, \Psi). \tag{67}$$

For periodic solutions, averaging over one period yields the time-averaged energy balance

$$\overline{g' J\left(\frac{\eta_2^2}{2}, \frac{H_1 H_2}{fH}\right)} - \overline{\eta_2 \, \mathrm{curl}\left(\frac{H_2 \tau}{fH}\right)} = \frac{H_1}{H^2} \overline{\eta_2 J(H, \Psi)}, \tag{68}$$

where the overbar denotes the average. In the flat-bottom case, the left-hand side and right-hand side of the above energy balance would vanish separately, but this is not true over topography. We time-average the conversion term in our periodic solutions at each point and then area-average it over $6° \times 5°$ boxes to eliminate small-scale features; the result is depicted in Fig. 23 for the wavemaker (left panel) and wind-forced cases (right panel). In all four solutions for the wavemaker case, the coupling term is seen to act as a sink of energy east of the ridge and as a source west of it. In the sink region, the phase lines of η_2 are nearly parallel to f/H contours, as anticipated in section 3b(2). Overall, the sink is greater than the source, so the coupling term contributes to dissipate the baroclinic mode. In the wind-forced case the coupling term is dominantly a source of energy, localized mainly in the southwestern part of the ridge. Its role as a sink appears sparse and negligible, though the negative values do occur mostly to the east of the ridge. Therefore, it contributes mainly to increase the energy of the baroclinic mode. In these two cases the source and sink regions roughly coincide but their strengths differ.
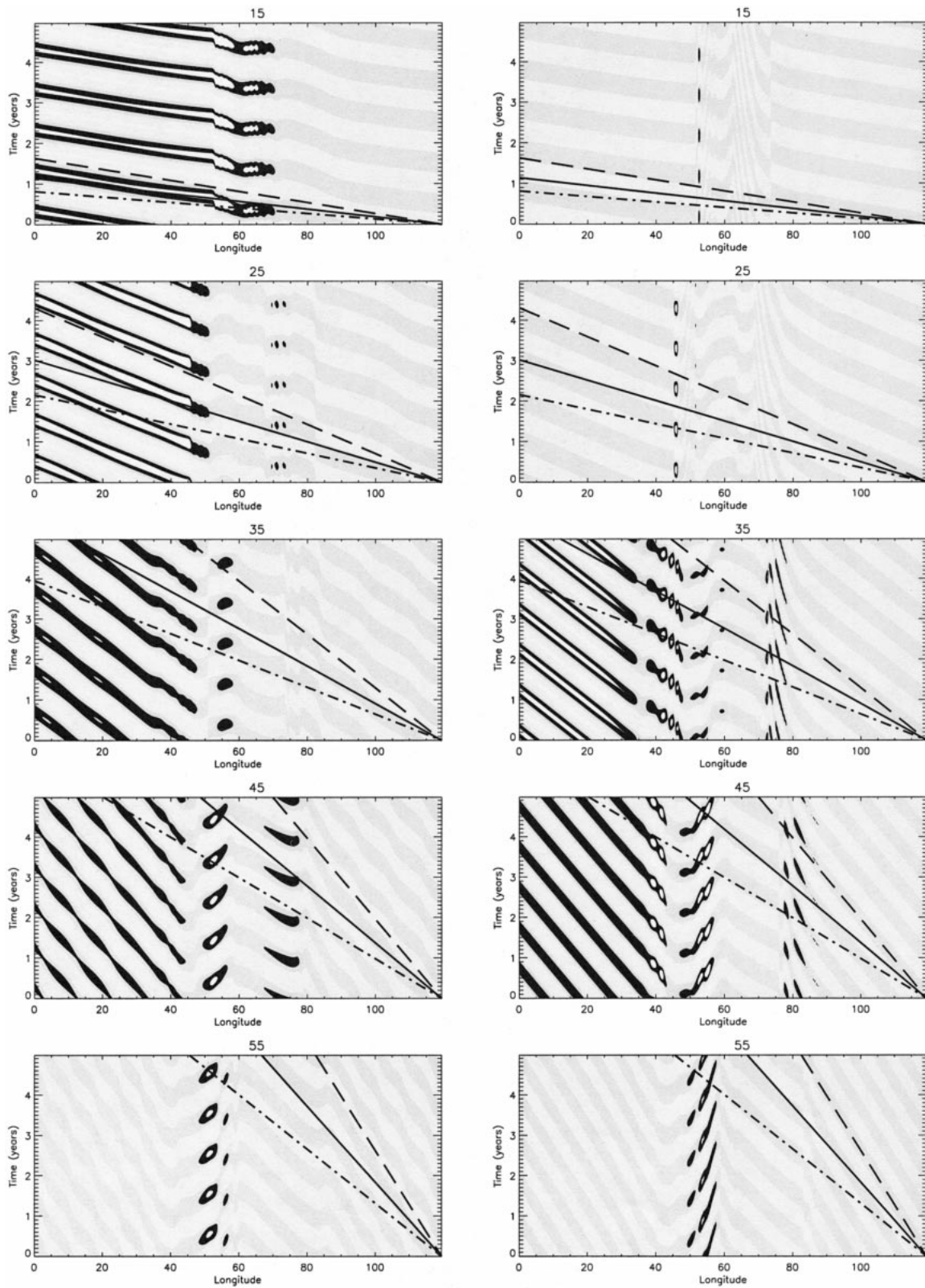
FIG. 20. Hovmöller diagrams for $\partial_x \eta_1$ (left) and $\partial_x \eta_2$ (right) every 10° latitude from 15°N (top) to 55°N (bottom), in the wind forced expt. with $\delta H = 2000$ m. Straight lines indicate propagation at the standard phase speed (dashed line), enhanced phase speed discussed in the text (solid line) and twice the standard phase speed (dotted–dashed line).
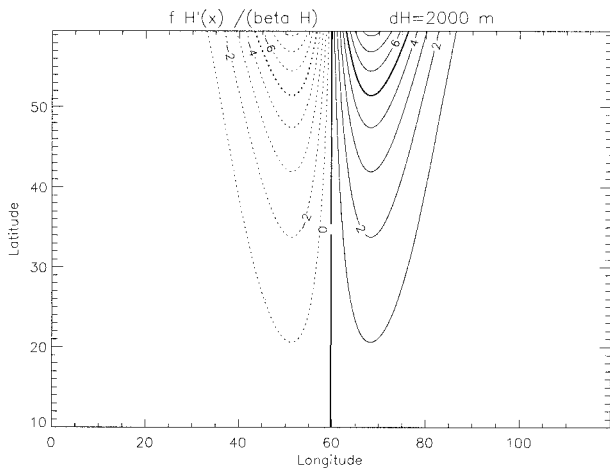
FIG. 21. Dimensionless parameter $\mu = fH'(x)/(\beta H)$ characterizing the steepness of the topography in the case $\delta H = 2000$ m.

f. Implications for sea level observations

In Chelton and Schlax (1996) sea level is low-pass filtered to remove the steric effect (i.e., the dominant zonally quasi-uniform effect due to seasonal heating and cooling). This filtering also reduces the impact of the barotropic mode and wind forced response whose zonal large-scale signatures may visually alter propagating signals in the same way as the steric effect. An alternative to the low-pass filter is to take the x derivative of the signal. Fig. 20 compares Hovmöller diagrams of $\partial_x \eta_1$ (left panel) versus $\partial_x \eta_2$ (right panel) depicted every $10°$ of latitude starting from $15°$N (from top to bottom) in the case $\delta H = 2000$ m. In the flat-bottom eastern and western regions, where propagation is well defined, the visual appearance between $\partial_x \eta_1$ and $\partial_x \eta_2$ is identical at all latitudes, with the propagation as predicted by the standard theory (indicated by the dashed line). This is not the case over the ridge for the plots at $15°$ and $25°$N where propagation is ill-defined and coincides with small values of the steepness parameter. Well-defined propagation over the ridge is observed only north of $25°$N, mostly on the ridge eastern flank where the steepness parameter is greater than unity. In these cases, $\partial_x \eta_1$ and $\partial_x \eta_2$ indicate similar propagation characteristics, with a phase speed intermediate between the elevated value $g'\beta H_1/f^2$ discussed in this paper (depicted as a solid line) and twice the standard speed (depicted as a dot–dashed line). From these examples, we conclude that it is well justified to regard the zonally low-pass filtered sea level as mimicking the behavior of first-mode baroclinic Rossby waves, although this does not seem to be true in regions where $\mu = O(1)$, a case that remains to be investigated.

6. Concluding remarks

a. Summary

Chelton and Schlax (1996) shows that major topographic features in the ocean influence the propagation speed and amplitude of baroclinic Rossby waves. We present here theoretical and numerical results from a two-layer model with wind-forced waves over strong topography. Our main theoretical result is an explicit expression for the evolution equation of the baroclinic mode in the special case where the topography varies linearly in longitude and the wind stress depends on latitude only. We also obtain an analytical expression in the case where the topography varies only with latitude for an arbitrary wind stress. These analytic results and additional numerical solutions with a midocean ridge indicate that steep topography alters the character of baroclinic Rossby waves in three primary ways.

1) PHASE SPEED ENHANCEMENT

Steep topography enhances systematically the phase speed of baroclinic Rossby waves by the factor $H/H_2 > 1$, compared to the standard flat-bottom speed, while hardly changing the westwardly directed, nondispersive behavior. In contrast, the propagation of barotropic Rossby waves can become strongly nonzonal as a result of topographic steering along the characteristics $f/H =$ const. These results are consistent with those in Rhines (1977) and Veronis (1981) for free waves. The phase speed amplification factor, H/H_2, is the same as the one arising in a pressure-compensated model, but it can occur in more general situations. Our numerical solutions reveal that pressure compensation does not always accompany enhanced propagation speed for a topography varying with longitude only, while we have shown analytically that it does in the case of a steep topography varying only with latitude. A more general condition for speed enhancement is that the lower-layer pressure zonal variations be uncorrelated to those of the layer interface.

2) ROSSBY WAVE GENERATION

Baroclinic Rossby waves are generated over a ridge in the case with wind forcing, while strongly dissipated in the case without it. Analysis of the coupling between the baroclinic and barotropic modes shows it to be a source of baroclinic energy in the former case and a sink in the latter case. In the forced case, the transfer of barotropic energy to the baroclinic mode occurs mainly in the southwestern part of the ridge. A simple analytical model mimicking the behavior of the baroclinic evolution equation over the ridge illustrates the wave creation.

3) ROSSBY WAVE DISSIPATION

Spatial variations in the bottom topography introduce a dissipation-like term in the evolution equation for the baroclinic mode, which is important only when the interfacial height contours are locally parallel to the contours $f/H =$ const. Analysis of the coupling between
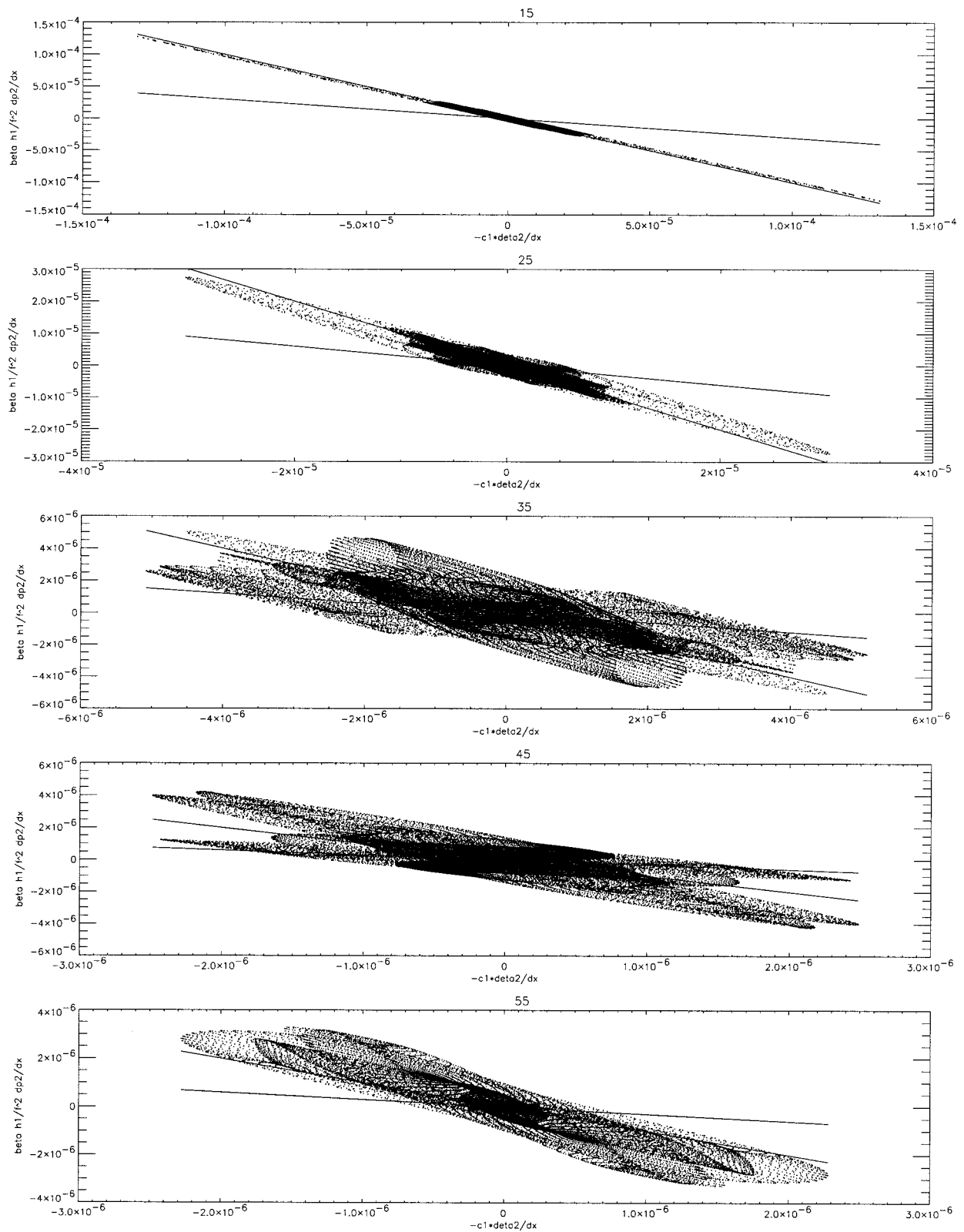
FIG. 22. Term $[\beta H_1/f^2]\partial p_2/\partial x$ vs $-[g'\beta H_1/f^2]\partial \eta_2/\partial x$. The two straight lines superimposed indicate the linear relations $\partial p_2/\partial x = [g'\partial \eta_2/\partial x$ (the less horizontal line) and $\partial p_2/\partial x = [g'(H_1/H)]\partial \eta_2/\partial x$ (the most horizontal line).
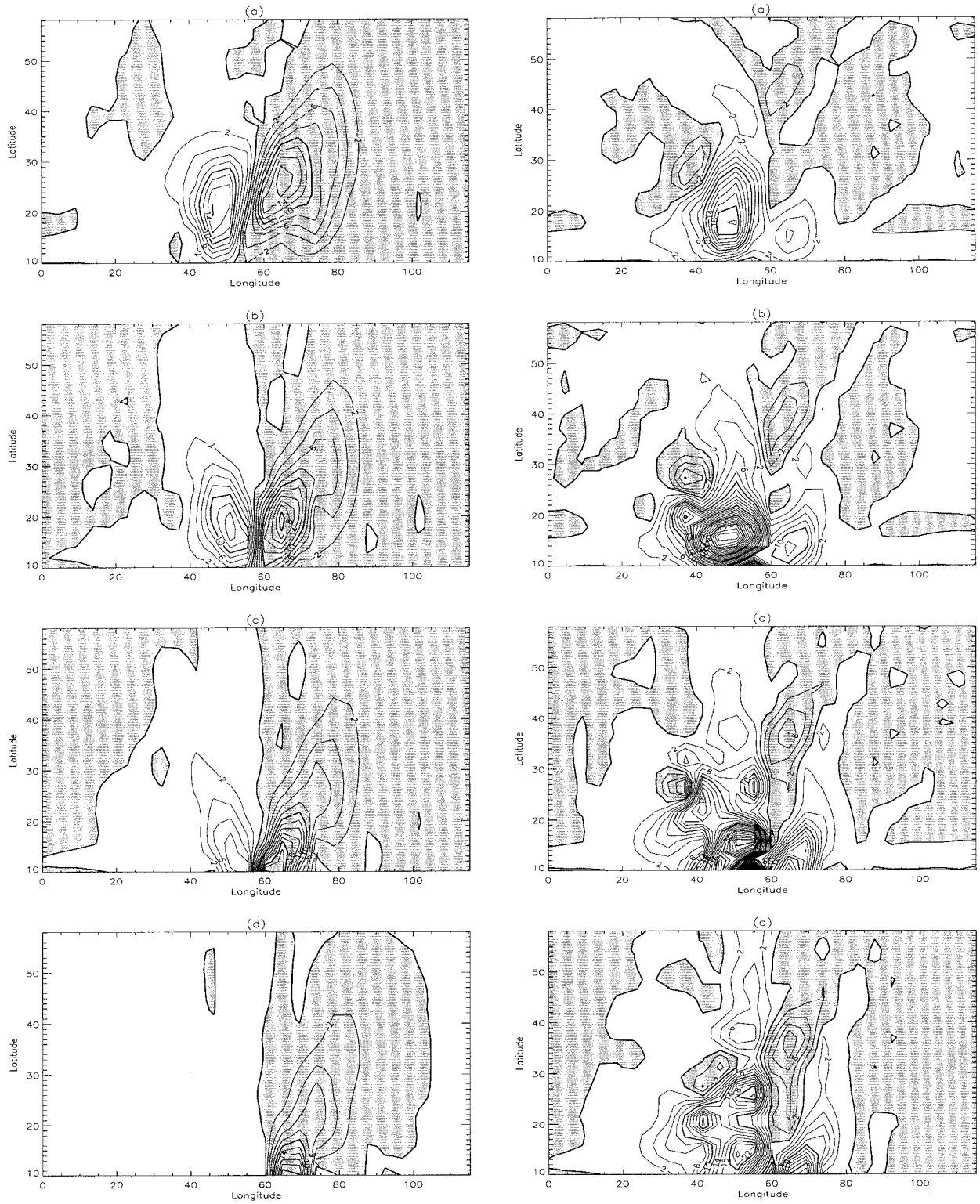
FIG. 23. Contribution of the coupling term $(H_1/H^2)\overline{J(H, \Psi)}$ in the time-averaged baroclinic energy balance for the wavameker experiments (left) and wind forced experiments (right): (a) $\delta H = 1000$ m, (b) $\delta H = 1500$ m, (c) $\delta H = 2000$ m, (d) $\delta H = 2500$ m. Negative values, indicating a sink of baroclinic energy, are shaded.

the barotropic and baroclinic mode confirms this view. In the wavemaker case, for instance, the coupling acts as a sink of baroclinic energy, on the eastward side of the ridge where the wave pattern is strongly correlated with the f/H contours. This term is interpreted as being responsible for the conversion of energy from the baroclinic to barotropic mode: it is dominant in the absence of external forcing and a strong barotropic mode and it causes the decrease of baroclinic amplitude across the ridge in our propagating eddy and baroclinic-wavemaker cases, as well as in the solutions of Sakamoto and Yamagata (1997). Topographic dissipation through mode coupling is an important additional mechanism to viscous decay (e.g., Qiu et al. 1997) for the decay of baroclinic Rossby waves in the ocean, and it does not rely on a parameter as poorly constrained as eddy viscosity.

b. Discussion

1) PATTERN DISTORTION

The primary cause of pattern distortion is due to the decrease with latitude of propagation speed of baroclinic Rossby waves. This is well illustrated in Fig. 4 of Chelton and Schlax (1996). There is a further cause from the spatially nonuniform conversion of energy to the barotropic mode, as well from dispersive effects [i.e., unequal phase and group velocities of baroclinic waves over topography (Straub 1994)], although those are weak over a steep topography (Rhines 1977; Veronis 1981).

2) COMPARISON WITH WKB SOLUTIONS

Killworth and Blundell (1999) addresses issues similar to those in this paper but in a completely different framework. It focuses on free waves in a continuously stratified ocean while we address wind-forced waves in a two-layer model, and it uses a WKB theory where we use direct integration. Our approach allows for energy scattering between modes and both steep and slowly varying topography. In our solutions the energy transfer between the barotropic and baroclinic modes is a primary influence on the behavior of baroclinic Rossby waves over topography: baroclinic waves would not be strongly dissipated during propagation over a ridge, and baroclinic Rossby waves would not be created west of ridge. In contrast, a WKB theory assumes that mode scattering is negligible, and Killworth and Blundell (1999) concludes that the topography has little effect on baroclinic Rossby waves.

3) PROSPECTS

A wind-forced, two-layer model seems to account, at least qualitatively, for enhanced phase speed and amplitude variations in the vicinity of major topographic features observed in the altimetric measurements of sea surface height. Still, a two-layer model is a crude representation of the actual stratification, and its predictions are quantitatively doubtful. In this respect the phase speed prediction is probably the more sensitive one since its enhancement ratio is H/H_2, whose continuously stratified analog is uncertain. On the other hand, the free-wave generation and dissipation rely on the form of the evolution equation for the first baroclinic mode, which is similar in two-layer and continuously stratified fluids. Our results allow some insight into the nature of the coupling between the barotropic and baroclinic modes over a variable topography, by providing some explicit expressions for the coupling in terms of localized dissipation and forcing. However, we believe that a wider range of topographic and forcing patterns should be examined beyond the simple configurations considered here (we hope to report on this later).

APPENDIX A

Approximation of $\mathcal{L}(\tilde{p})$

The operator $\mathcal{L}(\tilde{p})$ is defined in section 3b by

$$\mathcal{L}(\tilde{p}) = \mu\left[\frac{\partial \tilde{p}}{\partial y} - \int_{x_f}^{x} \frac{\partial}{\partial y}\left(\mu\frac{\partial \tilde{p}}{\partial y}\right)(x', y'(x'))\ dx'\right], \quad (A1)$$

with $y'(x')$ such that $\Pi(x', y'(x')) = $ const. The integral is decomposed as follows:

$$\int_{x_f}^{x} \frac{\partial}{\partial y}\left(\mu\frac{\partial \tilde{p}}{\partial y}\right)(x', y'(x'))\ dx'$$

$$= \int_{x_f}^{x} \mu\frac{\partial^2 \tilde{p}}{\partial y^2}(x', y')\ dx' + \int_{x_f}^{x} \frac{\partial \mu}{\partial y}\frac{\partial \tilde{p}}{\partial y}(x', y')\ dx'. \quad (A2)$$

Since $\mu = fH'(x)/\beta H(x)$, we have $\partial\mu/\partial y = H'(x)/H(x) = \beta\mu/f$. From scaling $\partial/\partial y$ by $1/\lambda$, the second term of (A2) is $O(f\lambda/\beta)$ compared to the first term, hence can be neglected assuming λ small compared to the planetary scale f/β.

Expressing $\tilde{p}$ in terms of its Fourier integral

$$\tilde{p} = \int_{-\infty}^{+\infty} \int_{-\infty}^{+\infty} \hat{p}(k, l)e^{i(kx+ly)}\ dk\ dl \quad (A3)$$

yields

$$\int_{x_f}^{x} \mu \frac{\partial^2 \tilde{p}}{\partial y^2}(x', y') \, dx'$$

$$= -\int_{-\infty}^{+\infty} \int_{-\infty}^{+\infty} \hat{p}(k, l) \int_{x_f}^{x} \mu l^2 e^{i(kx'+ly')} \, dx' \, dk \, dl. \quad \text{(A4)}$$

From $\Pi(x', y'(x')) = \text{const}$, it comes $dy'/dx' = -\partial_x \Pi / \partial_y \Pi = fH'(x)/(\beta H) = \mu$; hence $d(kx' + ly') = (k + l\mu)dx'$ so that

$$\int_{x_f}^{x} \mu l^2 e^{i(kx'+ly')} \, dx' = \int_{x_f}^{x} \frac{\mu l^2}{k + l\mu} e^{i(kx'+ly')}(k + l\mu) \, dx'$$

$$= -\int_{x_f}^{x} \frac{i\mu l^2}{k + l\mu} d(e^{i(kx'+ly')}). \quad \text{(A5)}$$

Integrating by parts yields

$$\int_{x_f}^{x} \mu l^2 e^{i(kx'+ly')} \, dx' = -\frac{i\mu l^2}{k + l\mu} e^{i(kx+ly)} + \frac{i\mu_f l^2}{k + l\mu_f} e^{i(kx_f+ly_f)}$$

$$+ \frac{f}{\beta H} \int_{x_f}^{x} \frac{\partial^2 H}{\partial x^2} \frac{ikl^2}{(k + l\mu)^2} e^{i(kx'+ly')} \, dx', \quad \text{(A6)}$$

using $(d\mu/dx')_{\Pi=\text{const}} = [f/(\beta H)]\partial^2 H/\partial x^2$ and assuming β constant (i.e., the β-plane approximation). Equation (A6) is estimated by approximating the characteristic curves by piecewise linear straight lines along which μ is constant. As a result, the path integral over the interval $[x, x_f]$ is split into $N - 1$ path integrals of the form:

$$I_n = \int_{x_n}^{x_{n+1}} \mu_n l^2 e^{i(kx'+ly')} \, dx'$$

$$= \frac{i\mu_n l^2}{k + l\mu_n}(e^{i(kx_n+ly_n)} - e^{i(kx_{n+1}+ly_{n+1})}). \quad \text{(A7)}$$

Assuming $\mu \gg 1$, two cases arise: case I, $k + l\mu_n \neq 0$: expanding the following term as a series in inverse powers of μ_n

$$\frac{\mu_n l^2}{k + l\mu_n} = l - \frac{k}{\mu_n} + o\left(\frac{1}{\mu_n}\right) \quad \text{(A8)}$$

yields

$$I_n = \left(\frac{\partial}{\partial y} - \frac{1}{\mu_n}\frac{\partial}{\partial x} + o\left(\frac{1}{\mu_n}\right)\right)(e^{i(kx_n+ly_n)} - e^{i(kx_{n+1}+ly_{n+1})}). \quad \text{(A9)}$$

case II, $k + l\mu_n \approx 0$: for a straight characteristic, we have $kx' + ly' = k(x' - x) + l(y' - y) + kx + ly = (k + l\mu)(x' - x) + kx + ly = kx + ly$; using $l \approx -k/\mu_n$, it follows that

$$I_n \approx \frac{k^2}{\mu_n}(x_{n+1} - x_n)e^{i(kx_n+ly_n)}$$

$$= -\frac{(x_{n+1} - x_n)}{\mu_n}\frac{\partial^2}{\partial x^2}e^{i(kx_n+ly_n)}. \quad \text{(A10)}$$

Reconstruction of the operator

Assuming the integral path to be comprised of a single straight line, we decompose the total wavenumber space into the two subdomains $\mathcal{D}_\varepsilon$ defined by $-\varepsilon \leq k + l\mu \leq \varepsilon$, $\varepsilon \ll 1$, and $\mathcal{D}_T$ its complement. As a result, using (A9) and (A10), noting that $(\partial_x + \mu\partial_y)\tilde{p}_\varepsilon = 0$ and hence that

$$\mu\frac{\partial \tilde{p}}{\partial y} = \mu\frac{\partial(\tilde{p}_T + \tilde{p}_\varepsilon)}{\partial y} = \mu\frac{\partial \tilde{p}_T}{\partial y} - \frac{\partial \tilde{p}_\varepsilon}{\partial x}, \quad \text{(A11)}$$

it comes

$$\mathcal{L}(\tilde{p}) = \mathcal{L}(\tilde{p}_\varepsilon) + \mathcal{L}(\tilde{p}_T), \quad \text{(A12)}$$

with

$$\mathcal{L}(\tilde{p}_T) = \int\int_{\mathcal{D}_T} \hat{p}(k, l)\mathcal{L}[e^{i(kx+ly)}] \, dk \, dl$$

$$\approx \frac{\partial \tilde{p}_T}{\partial x} + \left(\mu\frac{\partial \tilde{p}_T}{\partial y} - \frac{\partial \tilde{p}_T}{\partial x}\right)(x_f, y_f) \quad \text{(A13)}$$

$$\mathcal{L}(\tilde{p}_\varepsilon) = \int\int_{\mathcal{D}_\varepsilon} \hat{p}(k, l)\mathcal{L}[e^{i(kx+ly)}] \, dk \, dl$$

$$\approx -\frac{\partial}{\partial x}\left((x - x_f)\frac{\partial \tilde{p}_\varepsilon}{\partial x}\right). \quad \text{(A14)}$$

APPENDIX B

Approximation of $\mathcal{F}$

The forcing term $\mathcal{F}$, defined in section 3b, can be written under the form $\mathcal{F} = \mathcal{F}_1 + \mathcal{F}_2$ with

$$\mathcal{F}_1 = -\frac{\mu\beta H(x_f)}{H(x)}\frac{\partial \Psi}{\partial y}(x_f, y_f)$$

$$- \frac{\mu}{H}\int_{x_f}^{x} H(x')\frac{\partial}{\partial y} \text{curl}\tau \, dx' \quad \text{(B1)}$$

$$\mathcal{F}_2 = \frac{\beta\mu}{f}\left(\int_{x_f}^{x} \frac{\partial}{\partial y}(\mu\tau_y) \, dx' - \tau_y\right): \quad \text{(B2)}$$

$\mathcal{F}_1$ and $\mathcal{F}_2$ are estimated assuming 1) the topography varies linearly so that μ is constant along a characteristic and 2) the wind stress components depend on latitude only so that $\text{curl}\tau = -d\tau_x/dy$ and hence $\partial_y \text{curl}\tau =$

$-d^2\tau_x/dy^2$. Integrate by parts the integral term in $\mathcal{F}_1$, namely,

$$\frac{\mu}{H}\int_{x_f}^x H(x')\frac{\partial}{\partial y}\,\mathrm{curl}\tau\,dx'$$

$$= \mathrm{curl}\tau - \frac{H(x_f)}{H(x)}\,\mathrm{curl}\tau(y_f) - \frac{1}{H}\int_{x_f}^x \frac{\partial H}{\partial x}\,\mathrm{curl}\tau\,dx', \quad \text{(B3)}$$

using the result that for a function $g(y)$ we have $[d/dx']g(y') = [dg/dy](y')dy'/dx' = \mu[dg/dy](y')$. It follows that

$$\frac{1}{H}\int_{x_f}^x \frac{\partial H}{\partial x}\,\mathrm{curl}\tau\,dx' = -\frac{\beta}{f}\int_{x_f}^x \mu\frac{d\tau_x}{dy}\,dx'$$

$$= -\frac{\beta}{f}(\tau_x(y) - \tau_x(y_f)). \quad \text{(B4)}$$

As a result, the expression for $\mathcal{F}_1$ becomes

$$\mathcal{F}_1 = -\frac{\mu\beta H(x_f)}{H(x)}\frac{\partial\Psi}{\partial y}(x_f, y_f) + \frac{H(x_f)}{H(x)}\,\mathrm{curl}\tau(y_f)$$

$$- \mathrm{curl}\tau(y) + \frac{\beta}{f}(\tau_x(y) - \tau_x(y_f)). \quad \text{(B5)}$$

In order to evaluate $\mathcal{F}_2$, we first write

$$\int_{x_f}^x \frac{\partial}{\partial y}(\mu\tau_y)\,dx' = \int_{x_f}^x \mu\frac{d\tau_y}{dy}\,dx' + \int_{x_f}^x \frac{\partial\mu}{\partial y}\tau_y\,dx'$$

$$= \tau_y(y) - \tau_y(y_f) + \int_{x_f}^x \frac{\partial\mu}{\partial y}\tau_y\,dx', \quad \text{(B6)}$$

using the above remark for a function $g(y)$. To estimate the last term in (B6), note that $\partial\mu/\partial y = H'(x)/H(x) = \beta\mu/f$. Since $\beta\mu/f$ is constant in sign along the integral path, a classical theorem in integration theory allows us to write

$$\int_{x_f}^x \frac{\partial\mu}{\partial y}\tau_y\,dx' = \int_{x_f}^x \frac{\beta\mu}{f}\tau_y\,dx' = \tau_y(y^*)\int_{x_f}^x \frac{\mu\beta}{f}\,dx'$$

$$= \tau_y(y^*)\ln\!\left(\frac{f(y)}{f(y_f)}\right), \quad \text{(B7)}$$

with y^* an undetermined latitude comprised between y_f and y. As a result, $\mathcal{F}_2$ becomes

$$\mathcal{F}_2 = \frac{\beta\mu}{f}\left[\tau_y(y^*)\,\ln\!\left(\frac{f(y)}{f(y_f)}\right) - \tau_y(y_f)\right]. \quad \text{(B8)}$$

APPENDIX C

Analytical Solutions of the Forced Wave Equation

Exact solutions of the forced wave equation

$$\frac{\partial\tilde{p}}{\partial t} - c\frac{\partial\tilde{p}}{\partial x} = \mathcal{F}(x, t) \quad \text{(C1)}$$

are given for the two following forcing functions: smooth localized forcing:

$$\mathcal{F}(x, t) = \begin{cases} w_0\cos(\omega t), & |x - x_0| \geq l \\ \left[w_0 + \dfrac{\mu w_1}{2}\left(1 + \cos\!\left(\dfrac{\pi(x - x_0)}{l}\right)\right)\right]\cos(\omega t), \\ \hspace{4cm} |x - x_0| < l, \end{cases} \quad \text{(C2)}$$

abrupt localized forcing:

$$\mathcal{F}(x, t) = \begin{cases} w_0\cos(\omega t), & |x - x_0| \geq l \\ (w_0 + \mu w_1)\cos(\omega t), & |x - x_0| < l. \end{cases} \quad \text{(C3)}$$

These functions are depicted in Fig. 3. We define the three regions as

Region I: $\quad x_0 + l \leq x \leq x_E$

Region II: $\quad x_0 - l \leq x \leq x_0 + l$

Region III: $\quad 0 \leq x \leq x_0 - l.$

a. Solution for smooth forcing

$$\tilde{p}_{\mathrm{III}}(x, t) = \frac{w_0}{\omega}[\sin\omega t - \sin(\omega t + k(x - x_E))] \quad \text{(C4)}$$

$$\tilde{p}_{\mathrm{II}}(x, t) = \tilde{p}_{\mathrm{III}}(x, t) + \frac{\mu w_1}{2}\left[\frac{\sin\omega t}{\omega} + \frac{\omega}{\omega^2 - c^2\pi^2/l^2}\cos\!\left(\frac{\pi(x - x_0)}{l}\right)\sin\omega t + \frac{c\pi/l}{\omega^2 - c^2\pi^2/l^2}\sin\!\left(\frac{\pi(x - x_0)}{l}\right)\cos\omega t\right.$$

$$\left. + \frac{c^2\pi^2/l^2}{\omega(\omega^2 - c^2\pi^2/l^2)}\sin[\omega t + k(x - x_0 - l)]\right] \quad \text{(C5)}$$

$$\tilde{p}_{\mathrm{I}}(x, t) = \tilde{p}_{\mathrm{III}}(x, t) - \frac{\mu w_1}{\omega}\frac{c^2\pi^2/l^2}{\omega^2 - c^2\pi^2/l^2}\sin kl\,\cos[\omega t + k(x - x_0)]. \quad \text{(C6)}$$

b. Solution for abrupt forcing

$$\tilde{p}_{\mathrm{III}}(x,\ t) = \frac{w_0}{\omega}\{\sin(\omega t) - \sin[\omega t + k(x - x_E)]\} \quad (C7)$$

$$\tilde{p}_{\mathrm{II}}(x,\ t) = \tilde{p}_{\mathrm{III}}(x,\ t) + \frac{\mu w_1}{\omega}$$
$$\times \{\sin(\omega t) - \sin[\omega t + k(x - x_0 - l)]\} \quad (C8)$$

$$\tilde{p}_{\mathrm{I}}(x,\ t) = \tilde{p}_{\mathrm{III}}(x,\ t) + \frac{2\mu w_1}{\omega}\sin kl\,\cos[\omega t + k(x - x_0)].$$
$$(C9)$$

c. Amount of free waves generated

The free waves generated by the ridge are identified as the term proportional to μw_1 in $\tilde{p}_I(x,\ t)$. Their amplitude is given by

$$A_{\mathrm{smooth}} = -\frac{\mu w_1}{\omega}\frac{\sin(\pi k/k_T)}{(k/k_T)^2 - 1} \quad (C10)$$

$$A_{\mathrm{abrupt}} = \frac{2\mu w_1}{\omega}\sin(\pi k/k_T). \quad (C11)$$

Amplitudes A_{smooth} and A_{abrupt} are depicted in Fig. 4.

APPENDIX D

Energetics

Local and integral energy equations are derived for the two sets of variables $(\Psi, \tilde{p})$ and (p_1, p_2). The first set is used in our theoretical analysis in section 3, while the second is at the core of the numerical method described in section 5.

a. Barotropic–baroclinic formulation

Multiplying (6) by Ψ and (7) by η_2, recalling $\tilde{p} = g'\eta_2$, yields

$$J\!\left(\frac{f}{H},\frac{\Psi^2}{2}\right) = \Psi J\!\left(\frac{H_2}{H},\tilde{p}\right) - \Psi\ \mathrm{curl}\!\left(\frac{\tau}{H}\right) \quad (D1)$$

$$\frac{\partial}{\partial t}\frac{\eta_2^2}{2} - g'J\!\left(\frac{H_1 H_2}{fH},\frac{\eta_2^2}{2}\right) = \eta_2\ \mathrm{curl}\!\left(\frac{H_2\tau}{fH}\right) + \eta_2 J\!\left(\frac{H_2}{H},\ \Psi\right). \quad (D2)$$

Summing (D1) plus g' times (D2) yields

$$g'\frac{\partial}{\partial t}\frac{\eta_2^2}{2} - g'^2 J\!\left(\frac{H_1 H_2}{fH},\frac{\eta_2^2}{2}\right) + J\!\left(\frac{f}{H},\frac{\Psi^2}{2}\right)$$
$$= g'J\!\left(\frac{H_2}{H},\ \Psi\eta_2\right) - \Psi\ \mathrm{curl}\!\left(\frac{\tau}{H}\right) + g'\eta_2\ \mathrm{curl}\!\left(\frac{H_2\tau}{fH}\right). \quad (D3)$$

This equation is of the form

$$g'\frac{\partial}{\partial t}\frac{\eta_2^2}{2} - \mathrm{div}\mathcal{F}_E = -\Psi\ \mathrm{curl}\!\left(\frac{\tau}{H}\right) + \tilde{p}\ \mathrm{curl}\!\left(\frac{H_2\tau}{fH}\right) \quad (D4)$$

with $\mathcal{F}_E$, the energy flux, given by

$$\mathcal{F}_E = \frac{\beta}{2H}\!\left(\Psi^2 + \frac{H_1 H_2}{f^2}\tilde{p}^2\right)\hat{\mathbf{x}} + \frac{1}{2}\!\left(\frac{H_1\tilde{p} + f\Psi}{H}\right)^2\frac{\hat{\mathbf{z}}\times\boldsymbol{\nabla}H}{f}, \quad (D5)$$

or equivalently

$$\mathcal{F}_E = \frac{\beta H_1}{2f^2}\!\left(\frac{f\Psi - H_2\tilde{p}}{H}\right)^2\hat{\mathbf{x}} + \frac{1}{2}\!\left(\frac{H_1\tilde{p} + f\Psi}{H}\right)^2\hat{\mathbf{z}}\times\boldsymbol{\nabla}\!\left(\frac{H_2}{f}\right). \quad (D6)$$

The associated integral energy balance over the domain $\mathcal{D}$ is then given by

$$g'\frac{d}{dt}\iint_{\mathcal{D}}\frac{\eta_2^2}{2}\,dS = \oint_{\partial\mathcal{D}}\mathcal{F}_E\cdot\mathbf{n}\,dl + \iint_{\mathcal{D}}F_{\mathrm{wind}}\,dS \quad (D7)$$

$$F_{\mathrm{wind}} = \tilde{p}\ \mathrm{curl}\!\left(\frac{H_2\tau}{fH}\right) - \Psi\ \mathrm{curl}\!\left(\frac{\tau}{H}\right). \quad (D8)$$

b. Baroclinic, lower-layer pressure formulation

By summing (47) multiplied by p_2 plus (48) multiplied by $g'\eta_2$, we obtain

$$g'\frac{\partial}{\partial t}\frac{\eta_2^2}{2} - \frac{g'^2\beta H_1}{f^2}\frac{\partial}{\partial x}\frac{\eta_2^2}{2} - J\!\left(\frac{H}{f},\frac{p_2^2}{2}\right) + g'\frac{\beta H_1}{f^2}\frac{\partial}{\partial x}(p_2\eta_2)$$
$$= w_E(\tilde{p} - p_2). \quad (D9)$$

By using

$$J\!\left(\frac{H}{f},\frac{p_2^2}{2}\right) = \mathrm{div}\!\left[\frac{p_2^2}{2}\!\left(\frac{\hat{\mathbf{z}}\times\boldsymbol{\nabla}H}{f} + \frac{\beta H}{f^2}\hat{\mathbf{x}}\right)\right], \quad (D10)$$

Eq. (D9) becomes

$$g'\frac{\partial}{\partial t}\frac{\eta_2^2}{2} - \mathrm{div}\mathcal{F}_E = p_1 w_E \quad (D11)$$

with

$$\mathcal{F}_E = \frac{\beta}{f^2}\frac{H_1 p_1^2 + H_2 p_2^2}{2}\hat{\mathbf{x}} + \frac{p_2^2}{2}\frac{\hat{\mathbf{z}}\times\boldsymbol{\nabla}H}{f}, \quad (D12)$$

or equivalently

$$\mathcal{F}_E = \frac{\beta H_1}{2f^2}p_1^2\hat{\mathbf{x}} + \frac{1}{2}p_2^2\hat{\mathbf{z}}\times\boldsymbol{\nabla}\!\left(\frac{H_2}{f}\right). \quad (D13)$$

The resulting integral energy equation is given by

$$g'\frac{d}{dt}\iint_{\mathcal{D}}\frac{\eta_2^2}{2}\,dS = \oint_{\partial\mathcal{D}}\mathcal{F}_E\cdot\mathbf{n}\,dl + \iint_{\mathcal{D}}p_1 w_E\,dS. \quad (D14)$$

REFERENCES

Allen, J. S., and R. D. Romea, 1980: On coastal trapped waves at low latitudes in a stratified ocean. *J. Fluid Mech.,* **98,** 555–585.

Anderson, D. L. T., and A. E. Gill, 1975: Spin-up of a stratified ocean, with application to upwelling. *Deep-Sea Res.,* **22,** 583–596.

——, and P. D. Killworth, 1977: Spin-up of a stratified ocean with topography. *Deep-Sea Res.,* **24,** 709–732.

Barnier, B., 1988: A numerical study on the influence of the Mid-Atlantic Ridge on nonlinear first-mode baroclinic Rossby waves generated by seasonal winds. *J. Phys. Oceanogr.,* **18,** 417–433.

Chang, P., and S. G. H Philander, 1989: Rossby wave packets in baroclinic mean currents. *Deep-Sea Res.,* **36,** 17–37.

Charney, J. G., and G. R. Flierl, 1981: Oceanic analogues of atmospheric motions. *Evolution of Physical Oceanography,* B. A. Warren and C. Wunsch, Eds., The MIT Press, 504–548.

Chelton, D. B., and M. G. Schlax, 1996: Global observations of oceanic Rossby waves. *Science,* **272,** 234–238.

Colin de Verdière, A., 1988: Buoyancy driven planetary flows. *J. Mar. Res.,* **46,** 215–265.

de Szoeke, R. A., and D. B. Chelton, 1999: The enhancement of planetary wave speeds by homogeneous potential vorticity layers. *J. Phys. Oceanogr.,* **29,** 500–511.

Dewar, W. K., 1998: On ''too fast'' baroclinic planetary waves in the general circulation. *J. Phys. Oceanogr.,* **28,** 1739–1758.

Frankignoul, C., P. Müller, and E. Zorita, 1997: A simple model of the decadal response of the ocean to stochastic wind forcing. *J. Phys. Oceanogr.,* **27,** 1533–1546.

Hallberg, R., 1997: Localized coupling between the surface and bottom-intensified flow over topography. *J. Phys. Oceanogr.,* **27,** 977–998.

Killworth, P. D., and J. R. Blundell, 1999: The effect of bottom topography on the speed of long extratropical planetary waves. *J. Phys. Oceanogr.,* **29,** 2689–2710.

——, D. B. Chelton, and R. de Szoeke, 1997: The speed of observed and theoretical long extratropical planetary waves. *J. Phys. Oceanogr.,* **27,** 1946–1966.

Lighthill, J., 1978: *Waves in Fluids.* Cambridge University Press, 502 pp.

McWilliams, J. C., P. Gent, and N. Norton, 1986: The evolution of balanced, low-mode vortices on the β-plane. *J. Phys. Oceanogr.,* **16,** 838–855.

Mellor, G. L., and X. H. Wang, 1996: Pressure compensation and the bottom boundary layer. *J. Phys. Oceanogr.,* **26,** 2214–2222.

Milliff, R. A., and J. C. McWilliams, 1994: The evolution of boundary pressure in enclosed ocean basins. *J. Phys. Oceanogr.,* **24,** 1317–1338.

Philander, S. G. H., 1979: Equatorial waves in the presence of the equatorial undercurrent. *J. Phys. Oceanogr.,* **9,** 254–262.

Qiu, B., W. Miao, and P. Müller, 1997: Propagation and decay of forced and free baroclinic Rossby waves in off-equatorial oceans. *J. Phys. Oceanogr.,* **27,** 2405–2417.

Reznik, G. M., and T. V. Tsybaneva, 1994: On the influence of topography and stratification on planetary waves in the ocean (two-layer model) (English translation). *Oceanology,* **34,** 1–9.

Rhines, P. B., 1970: Edge-, bottom-, and Rossby waves in a rotating stratified fluid. *Geophys. Fluid Dyn.,* **1,** 273–302.

——, 1977: The dynamics of unsteady currents. *The Sea,* Vol. 6, E. Goldberg, Ed., Wiley, 189–318.

Sakamoto, T., and T. Yamagata, 1997: Evolution of baroclinic planetary eddies over localized bottom topography in terms of JEBAR. *Geophys. Astrophys. Fluid Dyn.,* **84,** 1–27.

Samelson, R. M., 1992: Surface-intensified Rossby waves over rough topography. *J. Mar. Res.,* **50,** 367–384.

Schlax, M. G., and D. B. Chelton, 1994: Detecting aliased tidal errors in altimeter height measurements. *J. Geophys. Res.,* **99,** 12 603–12 612.

Straub, D. N., 1994: Dispersion of Rossby waves in the presence of zonally varying topography. *Geophys. Astrophys. Fluid Dyn.,* **75,** 107–130.

Sverdrup, H., 1947: Wind-driven currents in a baroclinic ocean: With application to the equatorial currents of the eastern Pacific. *Proc. Natl. Acad. Sci. USA,* **33,** 318–326.

Tokmakian, R. T., and P. Challenor, 1993: Observations in the Canary basin and the Azores frontal region using GEOSAT data. *J. Geophys. Res.,* **98,** 4761–4773.

Veronis, G., 1981: Dynamics of large-scale circulation. *Evolution of Physical Oceanography,* B. A. Warren and C. Wunsch, Eds., The MIT Press, 140–183.

White, W. B., 1977: Annual forcing of baroclinic long waves in the tropical North Pacific Ocean. *J. Phys. Oceanogr.,* **7,** 50–61.

Zheng, Q., X.-H. Yan, C.-R. Ho, and C.-K. Tai, 1994: The effects of shear flow on propagation of Rossby waves in the equatorial oceans. *J. Phys. Oceanogr.,* **24,** 1680–1686.